

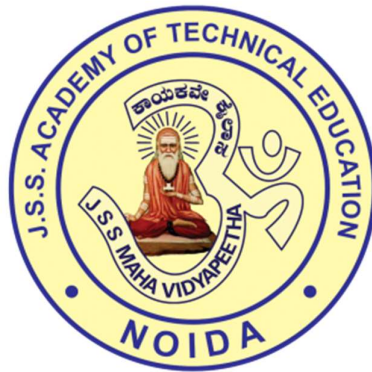
Project Report
On
STUDY OF TWO FREQUENCY PAUL TRAP

by

1. Shivansh Srivastav (1709131140)
2. Shivi Bisht (1709131142)
3. Shivendra Singh (1709131141)

Under the Guidance of

Mr. Anuranjan Kansal



Submitted to the Department of Electronics & Communication Engineering
in partial fulfillment of the requirements
for the degree of

Bachelor of Technology
in
Electronics & Communication Engineering

JSS Academy of Technical Education, Noida
Dr. A.P.J. Abdul Kalam Technical University, Lucknow

July – 2020-21

DECLARATION

We hereby declare that this submission is our own work and that, to the best of our knowledge and belief, it contains no material previously published or written by another person nor material which to a substantial extent has been accepted for the award of any other degree or diploma of the university or other institute of higher learning, except where due acknowledgment has been made in the text.

1. Shivansh Srivastav

Roll No: 1709131140

2. Shivi Bisht

Roll No: 1709131142

2. Shivendra Singh

Roll No: 1709131141

CERTIFICATE

This is to certify that Project Report entitled "**Study of Two Frequency Paul Trap**" which is submitted by **Shivansh Srivastav, Shivi Bisht and Shivendra Singh** partial fulfillment of the requirement for the award of B. Tech degree in Electronics and Communication Engineering of **Dr. A.P.J. Abdul Kalam Technical University, Lucknow** is a record of the candidate's own work carried out by him under my supervision. The matter embodied in this thesis is original and has not been submitted for the award of any other degree.

Anuranjan Kansal

(Assistant Professor)

Date:

ACKNOWLEDGEMENT

It gives us a great sense of pleasure to present the report of the B. Tech Project undertaken during B. Tech. Final Year. We owe special debt of gratitude to **Mr. Shivaji Sinha, Mr. Anuranjan Kansal**, Department of Electronics and Communication Engineering, J.S.S. Academy of Technical Education, Noida for his constant support and guidance throughout the course of our work. His sincerity, thoroughness and perseverance have been a constant source of inspiration for us. It is only his cognizant efforts that our endeavors have seen light of the day.

We also take the opportunity to acknowledge the contribution of **Dr Arun Kumar G** Head, Department of Electronics and Communication Engineering, J.S.S. Academy of Technical Education, Noida for his full support and assistance during the development of the project.

Signature :

Name : Shivansh Srivastav
Roll No. : 1709131140
Date :

Signature :

Name : Shivi Bisht
Roll No : 1709131142
Date :

Signature :

Name : Shivendra Singh
Roll No : 1709131141
Date :

ABSTRACT

We describe the operation of an electrodynamic ion trap in which the electric quadrupole field oscillates at two frequencies. This mode of operation allows simultaneous tight confinement of ions with extremely different charge-to-mass ratios, e.g., singly ionised atomic ions together with multiply charged nanoparticles. We derive the stability conditions for two-frequency operation from asymptotic properties of the solutions of the Mathieu equation and give a general treatment of the effect of damping on parametric resonances. Two-frequency operation is effective when the two species' mass ratios and charge ratios are sufficiently large, and further when the frequencies required to optimally trap each species are widely separated. This system resembles two coincident Paul traps, each operating close to a frequency optimized for one of the species, such that both species are tightly confined. This method of operation provides an advantage over single-frequency Paul traps, in which the weaker confined species forms a sheath around a central core of tightly confined ions. We verify these ideas using numerical simulations and by measuring the parametric heating induced in experiments by the additional driving frequency.

For our project, we wanted to build an oscillating system to trap charged particles. We decided to build a Paul trap, which is a form of ion trap that uses alternating electric fields to connect charged particles in the centre of the device. We were able to accomplish this using spherical brass electrodes, thick copper wires, a wire ring, and a step up transformer to give us the high voltage we needed from the wall. Our Paul trap worked very well, trapping charged plaster dust, which we illuminated with a bright green laser so that we could easily see the particles in the trap.

TABLE OF CONTENTS

Declaration	(ii)
Certificate	(iii)
Acknowledgement	(iv)
Abstract	(v)
List of Figures	(ix) - (xi)
Chapter 1: Introduction	1 - 4
1.1 Literature Review	1
1.2 Objective	2
1.3 Ion Trapping Physics	2
1.4 Earnshaw's Theorem	3
1.5 Confinement of Ions	4
Chapter 2: Types of Ion Traps	5 - 7
2.1 Planar Ion Trap	5
2.2 Quadrupole Ion Trap	5
2.3 Linear Ion Trap	6
2.4 Cylindrical Ion Trap	6
2.5 Ring Ion Trap	6
Chapter 3: Theory of Paul Trap	8 - 30
3.1 Theory of Paul Trap	8
3.1.1 Confinement of Two Species in a Single Freq. Paul Trap	10
3.2 Trapping with Two Frequencies	11

3.3	Paul Trap driven by Two Frequencies	11
3.4	Basic Trap Dynamics	14
3.4.1	Uniform Field Example	14
3.4.2	Add an Electric Field Gradient	16
3.5	Quadrupole Traps	19
3.6	The Triboelectric Series	23
3.7	Damped Ion Traps	25
3.7.1	Stokes Damping	26
3.7.2	Particle Dynamics in a Quadrupole Trap	28
Chapter 4: Experimental Apparatus		31 - 45
4.1	The Linear Trap Realization	31
4.1.1	Design and Fabrication	31
4.1.1.1	Holders	31
4.1.1.2	Electrodes	33
4.1.1.3	Position of Endcaps and Compensation Electrodes	34
4.1.1.4	Trap Assembly	34
4.1.2	Driving the Trap	35
4.1.2.1	DC Source	35
4.1.2.2	AC Source	36
4.1.2.3	Remote Control System	36
4.2	Particle Preparation and Loading Methods	36
4.2.1	Electrospray Ionization of Nanoparticles	37
4.2.2	Charging and Launching of Microparticles	38
4.3	Mathematical Background	39
4.4	Detection Schemes	41
4.4.1	Laser and Spatial Filter	41
4.4.2	Camera Detection	42
4.5	Data Analysis Tool	44

4.6	Materials Required	45
4.7	Setup	46
	4.7.1 Acrylic Box	46
	4.7.2 Electrode Setup	47
Chapter 5:	Experimental Results and Applications	48 - 53
5.1	Characterization of the Trap and Loading Methods	48
	5.1.1 Charge over Mass Measurements	48
5.2	Stability Diagrams	49
	5.2.1 Stability Diagram of the Microparticle	51
	5.2.2 Stability Diagram of the Nanoparticle	52
5.3	Results	53
5.4	Observations	53
5.5	Minimum Voltage Requirement	53
5.6	Oscillations	54
5.7	Challenges	54
5.8	Applications	54
	5.8.1 Paul Trap as a Spectrometer	54
	5.8.2 Precision Mass Measurement	54
	5.8.3 Quantum Jumps	55
	5.8.4 Quantum Computation	55
	5.8.5 Frequency Standard	55
	Conclusion and Outlook	56
	Appendix A	57 - 58
	Bibliography	59 - 62

LIST OF FIGURES

FIG. NO.	FIGURE TITLE	PG. NO.
1.1	Experimental Setup	3
2.1	Quadrupole Ion Trapping Schematic	5
2.2	Linear Ion Trap Schematic	6
2.3	Ring Trap Schematic	7
3.1	Ince-Strutt stability diagram for the Mathieu equation	9
3.2	Stability diagrams for a two-frequency-driven Paul trap	14
3.3	A charged particle placed initially at rest inside a parallel-plate capacitor	15
3.4	A charged particle placed initially at rest inside a curved-plate capacitor.	17
3.5	Method for making a 3D quadrupole ion trap	20
3.6	Another method for making a 3D quadrupole ion trap	20
3.7	The 3D quadrupole electric field geometry near the center of the Ring Trap	21
3.8	The 2D quadrupole electric field geometry near the center of the Linear Trap	23
3.9	The Triboelectric Series	24
4.1	Section view of the four rod Paul trap.	31

4.2	CAD drawing of one of the two identical holders for the Paul trap	32
4.3	Electrostatic simulations of E^2 arising from the geometrical configuration	33
4.4	The trap assembled in vertical configuration	34
4.5	Trap mounted on the optical table	35
4.6	Electrospray working principle.	37
4.7	Electric Field Configurations in Paul Trap	40
4.8	Alternating Electric Field	40
4.9	Photograph of scattered light from a trapped microsphere	41
4.10	Transverse laser mode at the input a) and output b) of the spatial filter image on a beam profiler.	41
4.11	Image of a trapped microsphere taken with the CMOS camera with a resolution of 1024x1024 pixels.	42
4.12	Nanosphere (a) and microsphere (b) scattered light recorded with the camera.	43
4.13	Schematic of the entire setup. The 650nm laser for imaging enters in the spatial lter that selects the TEM00 mode only.	43

4.14	This plot shows the pixel intensity (au) as a function of the pixel position along a vertical line passing on the two endcaps.	44
4.15	Picture of components.	45
4.16	Acrylic box setup	46
4.17	Electrode setup	47
5.1	Computer simulation of the axial electric field of the trap with an endcaps voltage of 15V.	49
5.2	Unstable (a) vs. stable (b) motion of a microsphere inside the trap captured by the camera.	49
5.3	Measured stability diagram of a single $21.8 \pm 0.9 \mu\text{m}$ microsphere trapped in air at a fixed frequency $\Omega = 2\pi \times 290 \text{ Hz}$.	51
5.4	Measured stability diagram of a trapped nanosphere at frequency $\omega'' = 2\pi \times 10 \text{ kHz}$.	52

CHAPTER - 1

INTRODUCTION

The quadrupole ion trap, or the Paul trap in honour of its inventor Wolfgang Paul who for which claimed the 1989 Nobel Prize, is a device that can confine charged particles using interactions between electric fields. Due to Earnshaw's theorem, we know that charged particles cannot be trapped stably by static electric fields alone. There are several different methods for trapping charged particles, and the Paul trap accomplishes this using AC voltage to generate alternating electric fields on a pair of hyperbolic electrodes (in our case, two brass spheres), suspended on either side of a ring electrode (a simple wire ring in our setup). This setup, when the hyperbolic electrodes are connected such that the hyperbolic electrodes are always at the same potential, and with opposite polarity of the ring electrode, generates an electric field that is zero at the centre of the ring and everywhere else provides a time averaged restoring force back towards the centre of the ring. This allows us to trap our charged particles within the ring. Ion traps are useful because they allow us to isolate individual charged particles over long periods of time, which we can then observe and use in experiments. This is much easier than attempting to gather data on a moving particle, and enables observation of particles that would otherwise be unobservable. Ion traps are also useful for controlling quantum states, and can be used in mass spectrometry and quantum computing.

1.1 LITERATURE REVIEW

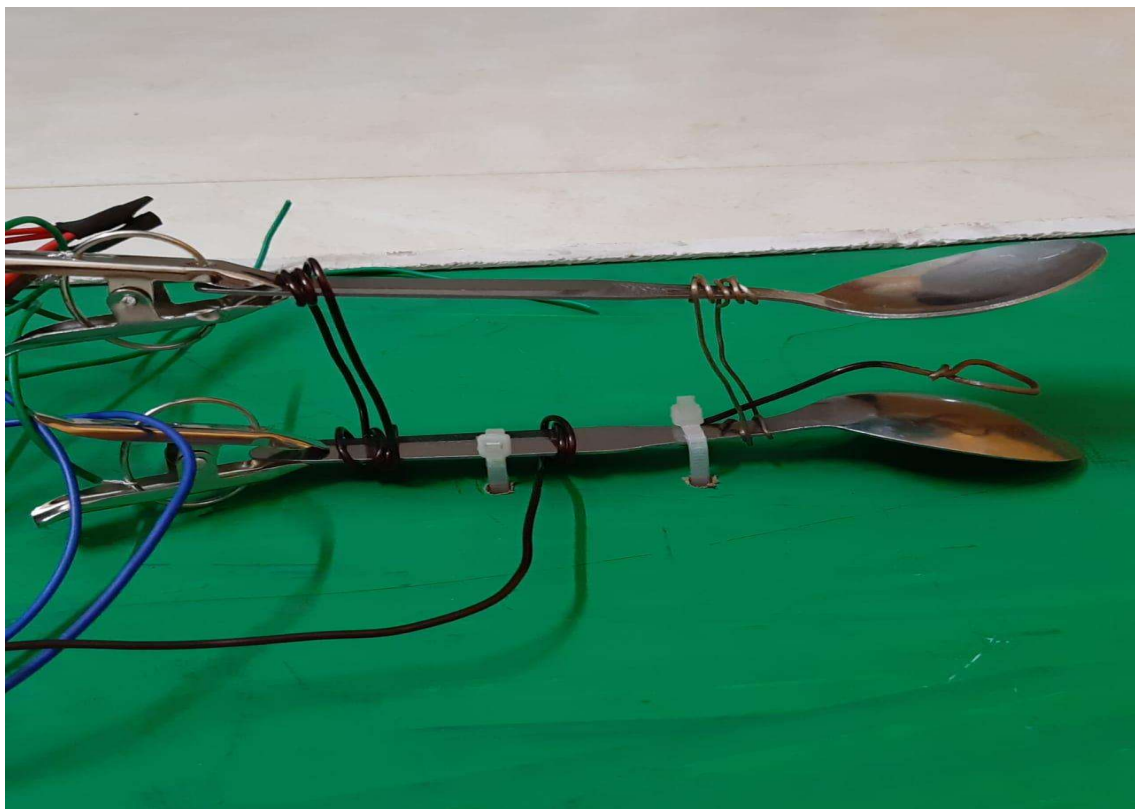
Electrodes are strategically shaped and placed for desired electric field interactions. In this setup, the spherical brass balls are at the opposite potential of the ring electrode. The electric field then oscillates between two configurations at a frequency of 60 Hz, which is the frequency of the wall voltage. One of the configurations stretches the particles that are outside the centre of the ring in the vertical direction and provides a restoring force towards the centre in the horizontal direction, and the other configuration is the opposite, the particles are stretched horizontally, and there is a restoring force toward the centre in the vertical direction. The rapid oscillation of the electric field between the two configurations provides an average confining force in all directions, because the trap field oscillates faster than the particles can escape the trap. Once particles settle into a place, they essentially oscillate in a fixed position very quickly. The oscillating and stretching in the horizontal and vertical directions cause the shape of the dust that we observe.

1.2 OBJECTIVE

To construct a Paul Trap model using commercially available tools and materials based on Ion trapping to observe the physics behind Ion Trapping and to study the particle dynamics under a high electric field. This setup also serves as a potential oscillating system. Particle motion will be observed under Laser light illuminance.

1.3 ION TRAPPING PHYSICS

An ion trap is a combination of electric or magnetic fields used to capture charged particles (ions) often in a system isolated from an external environment. Ion traps have a number of scientific uses such as mass spectrometry, basic physics research, and controlling quantum states. The basic idea of an ion trap is to confine a charged particle in free space, away from any other matter, using electric fields alone. There is a famous theorem, called Earnshaw's theorem, stating that one cannot construct a stable ion trap using electrostatic fields alone.



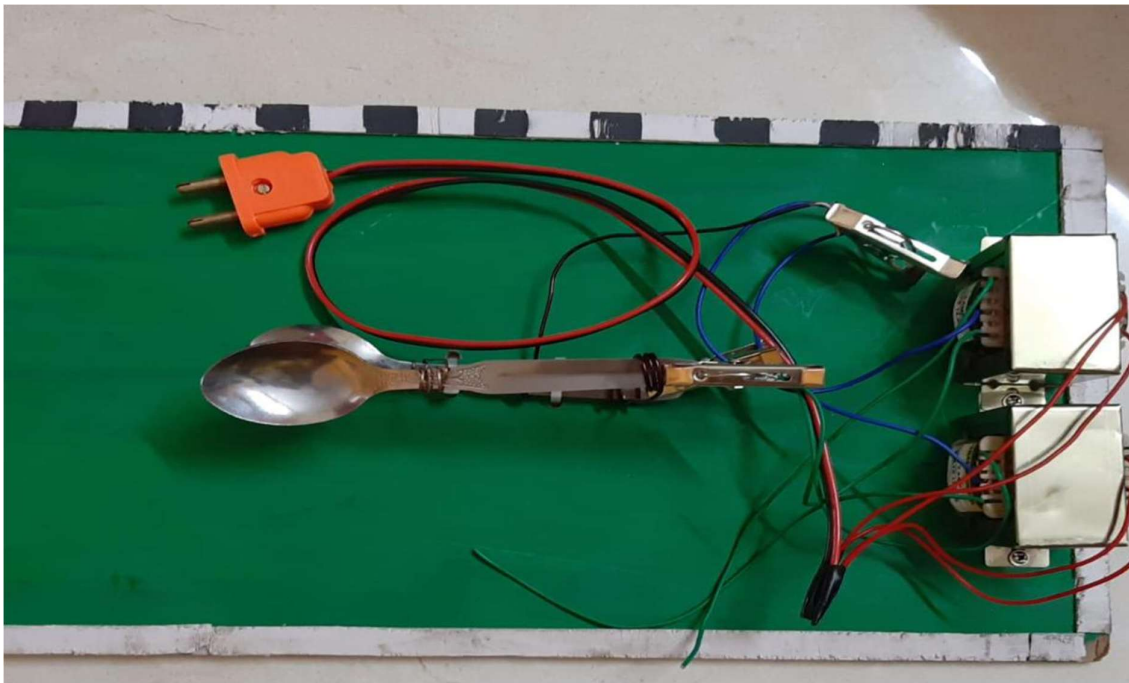


FIGURE 1.1 Experimental Setup (a) Front View (b) Top View

1.4 EARNSHAW'S THEOREM

The basic idea of an ion trap is to confine a charged particle in free space, away from any other matter, using electric fields alone. There is a famous theorem, called Earnshaw's theorem, stating that one cannot construct a stable ion trap using electrostatic fields alone. To trap a positively charged particle at some position in space, for example, the electric field vectors around that position would all have to be pointing inward. And Maxwell's equations, specifically Gauss's Law, tell us that this is impossible unless there is a net negative charge at that position. So, try as one might, fundamental laws of physics tell us that it is not possible to create a static electric field geometry that will stably trap charged particles in free space. There are magnetic variations of Earnshaw's theorem as well, for example stating that you cannot stably trap a bar magnet in free space using only static magnetic fields. Adding gravity does not help, and another version of Earnshaw's theorem states that you cannot levitate a stationary permanent magnet using only static magnetic fields. Fortunately, there are many routes around Earnshaw's theorem. One popular engineering method is to use active feedback. For the magnetic case, one can continually measure the position of a levitated magnet and adjust the forces appropriately to keep the magnet positioned where you want it. This method is relatively cheap and easy to implement, and magnetically levitated trains work this way. Another way around Earnshaw's theorem for magnetic levitation is to use a spinning magnet instead of a

stationary one. There is a toy called the Leviton (easily found online) that demonstrates levitation of a spinning magnet without using active feedback.

1.5 CONFINEMENT OF IONS

The purpose of an atom or ion trap is to confine the motion of the atomic or ionic particles to a small region of space. The trapping of charged particles, which is understandably far easier than the confinement of neutral atoms, as the forces which can be exerted by electromagnetic fields on the latter are far smaller. How does one go about trapping an ion? The simplest solution is to have the ion elastically bound to an origin by a restoring force F that increases linearly with the distance r ,

$$F = -kr$$

If the ion moves back and forth about an equilibrium position through

CHAPTER - 2

TYPES OF ION TRAPS

2.1 PLANAR ION TRAP

Quadrupole traps can also be "unfolded" to create the same effect using a set of planar electrodes. This trap geometry can be made using standard micro-fabrication techniques, including the top metal layer in a standard CMOS microelectronics process and is a key technology for scaling trapped ion quantum computers to useful numbers of qubits.

2.2 QUADRUPOLE ION TRAP

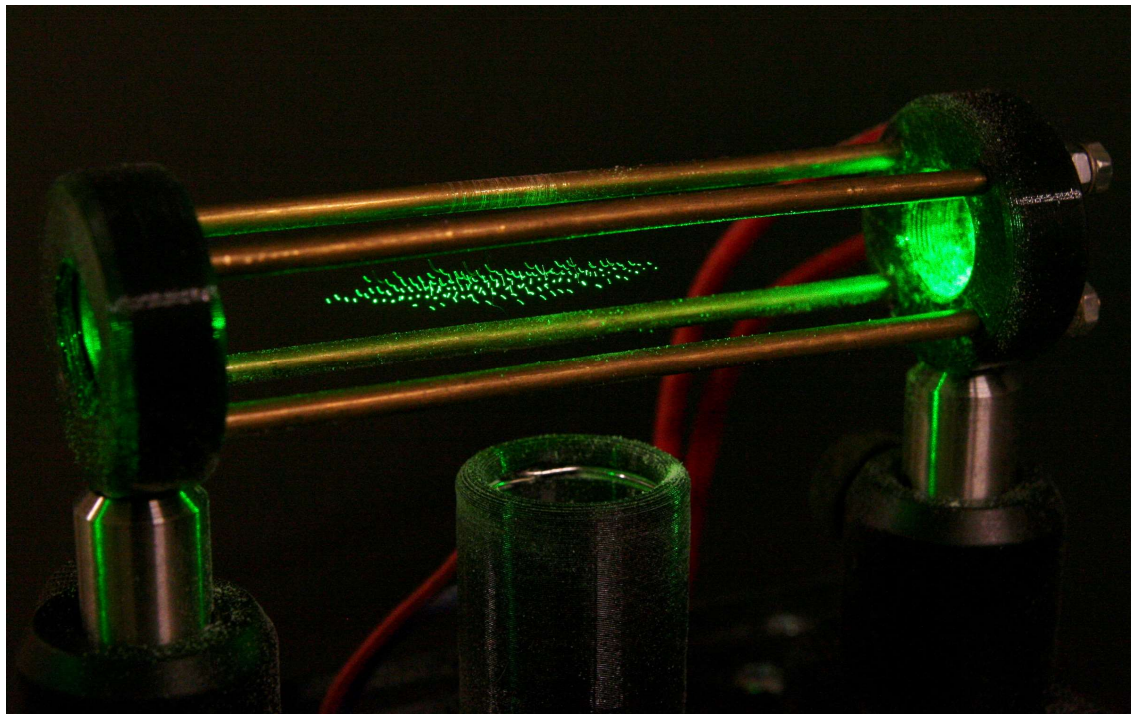


FIGURE 2.1 Quadrupole Ion Trapping Schematic

A **quadrupole ion trap** is a type of ion trap that uses dynamic electric fields to trap charged particles. They are also called radio frequency (RF) traps or Paul traps in honour of Wolfgang Paul, who invented the device and shared the Nobel Prize in Physics in 1989 for this work. It is used as a component of a mass spectrometer or a trapped ion quantum computer.

The quadrupole is the simplest electric field geometry used in such traps, though more complicated geometries are possible for specialized devices. The electric fields are generated from electric potentials on metal electrodes. A pure quadrupole is created

from hyperbolic electrodes, though cylindrical electrodes are often used for ease of fabrication. Microfabricated ion traps exist where the electrodes lie in a plane with the trapping region above the plane. There are two main classes of traps, depending on whether the oscillating field provides confinement in three or two dimensions. In the two-dimension case (a so-called "linear RF trap"), confinement in the third direction is provided by static electric fields.

2.3 LINEAR ION TRAP

The linear ion trap uses a set of quadrupole rods to confine ions radially and a static electrical potential on-end electrodes to confine the ions axially. The linear form of the trap can be used as a selective mass filter, or as an actual trap by creating a potential well for the ions along the axis of the electrodes. Advantages of the linear trap design are increased ion storage capacity, faster scan times, and simplicity of construction (although quadrupole rod alignment is critical, adding a quality control constraint to their production).

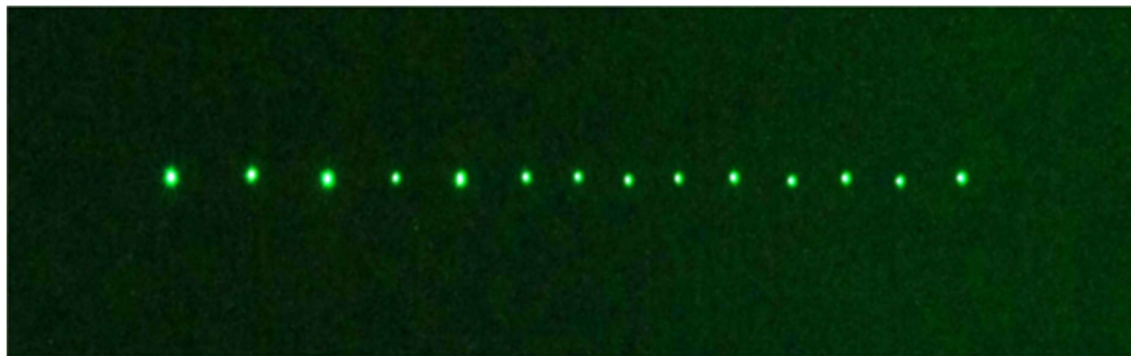


FIGURE 2.2 A row if ions stably held in the Linear Trap. The spacing between particles is approximately 1mm.

2.4 CYLINDRICAL ION TRAP

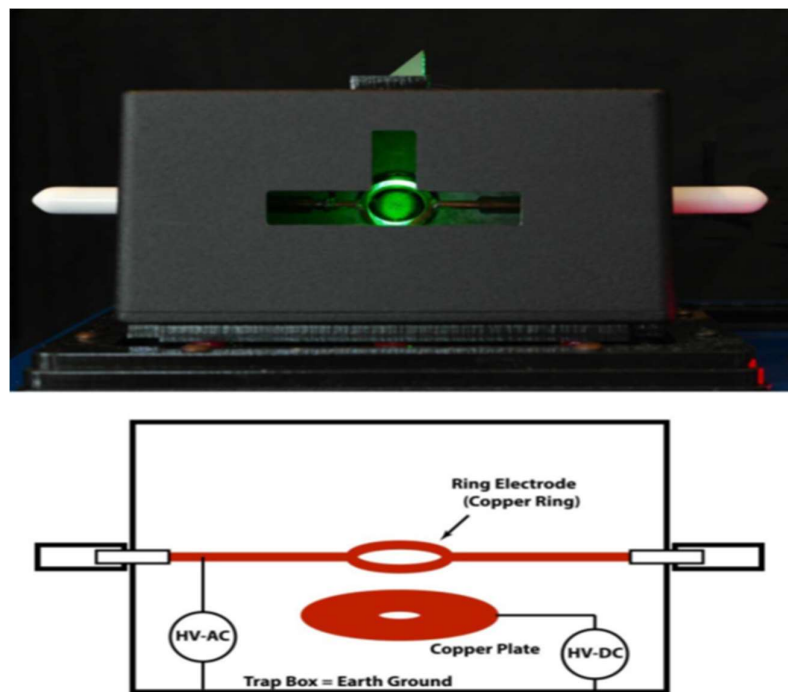
Ion traps with a cylindrical rather than a hyperbolic ring electrode have been developed and microfabricated in arrays to develop miniature mass spectrometers for chemical detection in medical diagnosis and other fields.

2.5 RING TRAP

The main element of the Ring Trap is a copper ring, with an inner diameter of 16 mm, that is connected to the AC high voltage (HV-AC), providing up to 6 kV at 60 Hz. The electric field configuration near the center of the ring is approximately that of a 3D quadrupole, and particles are trapped near the ring center. Static electric fields are also applied using the lower copper

plate (connected to HV-DC). The ring can be rotated about the horizontal axis shown, to provide different views of the trapped particles, and to observe gravitation and static electrical influences on the trap. The Ring Trap is surrounded by a grounded metal enclosure, with cut-outs for loading and observing the particles.

FIGURE 2.3 (Top) The Ring Trap, with a large (green) cloud of trapped ions. **(Bottom)** A schematic diagram of the Ring Trap. The side handles are for rotating the ring electrode.



CHAPTER 3

THEORY OF PAUL TRAP

3.1 THEORY OF PAUL TRAP

Newton's equation of motion for a particle of mass M and electric charge Q along the y-axis of a Paul trap is

$$M(\ddot{y} + \Gamma\ddot{y}) = Q E_y(t),$$

where Γ is a damping constant.

The time-dependent force equals the charge Q times the component of the electric field E_y along this axis. The quadrupole field is

$$E_y(t) = V(t) y/r_0^2$$

where the distance r_0 characterises the electrodes spacing, and the applied voltage is $V(t) = V_0 + V \cos(\Omega t)$. A change of variables $\Omega t = 2\tau$ transforms the equation of motion into the Mathieu equation

$$\frac{d^2y}{d\tau^2} + [a - 2q \cos(2\tau)] y(\tau) = 0,$$

with $a = (Q/M\Omega^2)^*4V_0/r_0^2$ and $q = -(Q/M\Omega^2)^*2V/r_0^2$. An approximate method that elucidates the behaviour of the Paul trap for certain parameters shows that the motion of the ion consists of an oscillation at a slow secular frequency plus a fast, small-amplitude micromotion at the driving frequency:

$$y = A \cos(\omega t)(1 + 0.5*q \cos(\Omega t)).$$

The slow motion is that of a particle in a harmonic pseudopotential with secular frequency w given by the Dehmelt approximation

$$\omega = \frac{\Omega}{2} \sqrt{a + \frac{1}{2}q^2}.$$

More generally, the motion of charged particles in an oscillating electric field may be described by a ponderomotive potential that is proportional to the square of the amplitude of the oscillating electric field. The stability region of the one-dimensional Mathieu equation is shown in Figure 3.1(a).

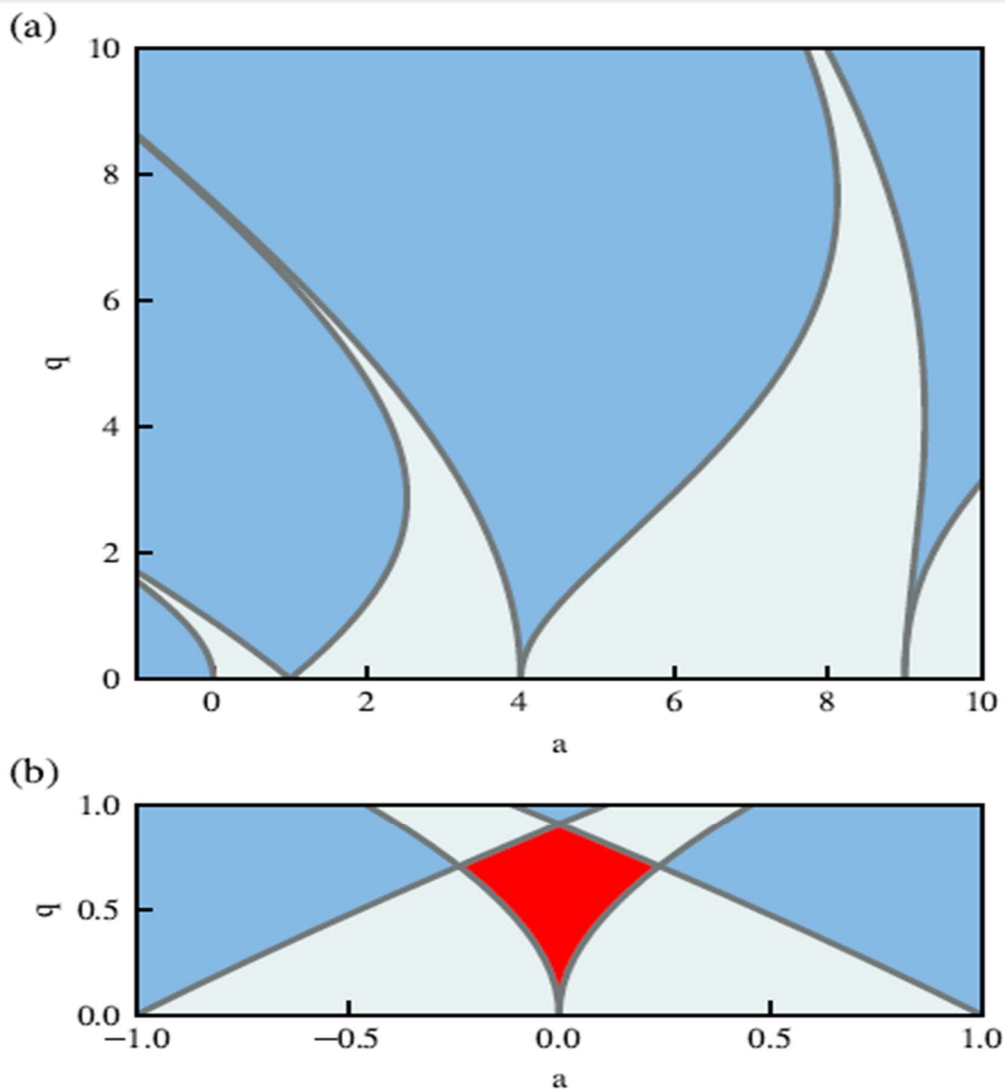


FIGURE 3.1 (a) Ince-Strutt stability diagram for the Mathieu equation. The solutions are stable and periodic in the lightly coloured areas and diverging otherwise. (b) The stability region for a linear Paul trap, shown in red, is the overlap of the stability region for motion along the x- and y- axes. A linear quadrupole field has reflection symmetry along the line $a = 0$ since $a_y = -a_x$.

Stability in both x- and y-axes is independent of the sign of q , and hence the sign of the charge Q . The Paul trap is stable when $q > 0$ even for negative values of a since a small amount of anti-trapping by the static electric field can be overcome by the pseudopotential, e.g., for $q = 0.4$ stable solutions exist for $|a| < 0.09$. Figure 3.1(b) shows the intersection of the stability regions for motion in the x and y directions of a linear Paul; values of the parameters a and q within this overlap region give stable confinement. In a linear Paul trap, the motion of the ion is stable over the range $0 < q < 0.91$ for $a = 0$.

Values of $q \leq 0.4$ give robust operation of a Paul trap without anharmonic effects that tend to destabilise the confinement at higher values. Therefore we use $q = 0.4$ as a typical value throughout this paper, although the results do not depend on the exact value chosen. Practical considerations limit the attainable curvature $V''_{\text{max}} = V/r_0^2$ for a given trap. Realistic values are $V = 500$ V and $r_0 = 0.5$ mm giving $V''_{\text{max}} = 2 \times 10^9$ V/m² which is comparable to the value used in the measurements. This choice of V''_{max} determines the driving frequency that gives a suitable value of the q -parameter, i.e., $q = 0.4$.

3.1.1 CONFINEMENT OF TWO SPECIES IN A SINGLE-FREQUENCY PAUL TRAP

We consider two species A, B trapped in a Paul trap, species A is atomic **138Ba**⁺ and B a heavy ion with $M_B = 1.4 \times 10^6$ Da and $Q_B = +33e$. The spring constant $\kappa = M\omega^2$ determines the extent of the ion cloud y_{rms} at temperature T , and hence the overlap of the two species, since by the equipartition theorem $k_B T = k y_{\text{rms}}^2$. At low T the ions form Coulomb crystals and electrostatic repulsion determines their spatial extent: equal and opposite trapping forces between two ions $k_A y_A = -k_B y_B$ result in similar displacements, $|y_A| \approx |y_B|$, if the spring constants are similar $k_A \approx k_B$. For most of these calculations it is not necessary to consider the Coulomb interaction of the trapped ions, however it is included in the numerical simulations. In the pseudopotential approximation the spring constant is where $\omega = q\Omega / \sqrt{8}$ when $a = 0$. The ratio of the two spring constants for the single-frequency trap is:

$$\left[\frac{\kappa_B}{\kappa_A} \right]_{\text{lrf}} = \frac{\kappa_B(\Omega)}{\kappa_A(\Omega)} = \frac{Q_B^2/M_B}{Q_A^2/M_A},$$

$$\kappa \approx M\omega^2 = \frac{1}{8} \cdot \frac{-\omega^2}{r_0^2} = \frac{\tilde{M}\Omega^2}{M\Omega^2} \cdot \left(\frac{1}{2r_0^2} \right)^2,$$

where $\kappa_A(\Omega)$, $\kappa_B(\Omega)$ are both functions of Ω . For the species considered here $(Q_B^2/M_B)/(Q_A^2/M_A) = 0.1$, so that the confinement of species B is less tight; these ions move to the outside of the cloud of species A in a single-frequency trap since $q \ll Q/M$ for fixed Ω , and $q_A = 0.4$ for species A implies $q_B = 0.001$.

The spring constant of a Paul trap operating at a fixed voltage V , and with drive frequency optimized such that $q = 0.4$, depends only on the ion's charge. If it were possible to simultaneously achieve the same conditions for both species, the ratio of their spring constants would be $\kappa_B/\kappa_A = Q_B/Q_A \gg 1$, which is opposite to normal for a Paul trap. However, this

scenario cannot be attained in a single frequency trap. The constraints that $q = 0.4$ for fixed V are incompatible for the two species, each requiring a different drive frequency. Much of this work is devoted to optimisation of the confinement of species B, to give the maximum k_B , subject to the constraint that species A remains trapped. We show that two-frequency operation gives significant improvement over a single-frequency Paul trap in suitable circumstances.

3.2 TRAPPING WITH TWO FREQUENCIES

We can optimise the confinement of each species individually by using different driving frequencies: a high frequency Ω_n for the light ions and a low frequency Ω for the heavier ones. Applying the second, lower frequency field augments the confinement of the heavier species. The ratio of spring constants now becomes

$$\left[\frac{\kappa_B}{\kappa_A} \right]_{2\text{rf}} = \frac{\kappa_B(\Omega)}{\kappa_A(\Omega_n)} = \left(\frac{V_1}{\Omega} \cdot \frac{\Omega_n}{V_n} \right)^2 \frac{Q_B^2/M_B}{Q_A^2/M_A},$$

where V_1, V_n are the voltages that correspond to Ω, Ω_n . Comparison with above eq. shows that there is an enhancement by a factor of $\{(\Omega_n/\Omega)^2\} * \{(V_1/V_n)^2\}$, which can be much greater than unity as shown below. Although $V_1 \ll V_n$ because the low-frequency component strongly influences the stability of species A, an overall enhancement can be achieved when $\Omega_n/\Omega \gg 1$ is sufficiently large.

To configure the two-frequency trap we first set the values V_n, Ω_n to be optimal for single frequency confinement of the light ion with $q_A = 0.4$. With species A now well confined, we chose parameters Ω, V_1 to trap species B, subject to the requirement that there is no parametric excitation of A. This approach ensures that both species are stable in the two-frequency quadrupole field.

3.3 PAUL TRAP DRIVEN BY TWO FREQUENCIES

Paul traps have been typically used to investigate the properties of trapped objects such as a cloud of ions. For a system like an ion cloud with many degrees of freedom, an additional quadrupole field with lower amplitude than the primary one can be scanned while fluorescence of the ions is registered, leading to the appearance of various mechanical resonances. These resonances are mostly due to parametric excitations of the secular frequencies, higher-order modes of oscillation and nonlinearities of the trap potential. Thus, in these kinds of measurements, the second oscillating field is used to probe the system.

To understand the effect of this second field, we rewrite Eq. (2.1.29) taking into account a second driving with a different frequency and amplitude but with the same field geometry.

The equation of motion is now given by:

$$m\ddot{x} = -\gamma\dot{x} + \left(\frac{QU_{end}}{z_0^2} + \frac{QU_{off}}{z_0^2} + \frac{QU_1}{r_0^2} \cos(\Omega_1 t) + \frac{QU_2}{r_0^2} \cos(\Omega_2 t) \right)x,$$

where γ is the damping constant, m and Q are the mass and the charge of the trapped particle and U_i , Ω_i for $i = \{1, 2\}$ are the amplitude and the frequency of the first and the second oscillating potential, respectively. In order to simplify the calculations, we consider the second frequency Ω_2 to be a harmonic of the first one, so that $\Omega_2 = n\Omega_1$ with n an integer. For this reason, Ω_1 and Ω_2 will be called the slow frequency and the fast frequency respectively.

With the same transformation used in Eq. (2.1.9), we can recast the above equation of motion (2.2.1) as

$$\frac{d^2x}{dt_1^2} + 2b_1 \frac{dx}{dt_1} + (a_x - 2q_x \cos(2t_1) - 2p_x \cos(2nt_1))x = 0,$$

where we have additionally used

$$p_x = \frac{2QU_2}{mr_0^2\Omega_1^2},$$

$$\Omega_2 = n\Omega_1,$$

and where the index in b_1 emphasizes that we have rescaled the time with respect to the slow frequency such that $b_1 = \gamma/(m\Omega_1)$.

Eq. (2.2.2) is a second-order linear ordinary differential equation with periodic coefficients, generally known in the literature as the Hill equation of which the Mathieu equation (2.1.8) is just one particular case involving a single frequency.

As was done for the Mathieu equation, we use Floquet theory to find an analytic solution to Eq. (2.2.2) in terms of an infinite series expansion by substituting the ansatz (2.1.14) in (2.2.2) we get a recursive relation for find the β_x parameter, namely

Eq. (2.2.2) has bounded and unbounded solutions in time, just as its single-frequency counterpart does, and these solutions depend on the particular values assumed by its β_x parameter. The boundary between stable and unstable motion is represented (for a fixed value

$$C_{2r} + D_{2r}[C_{2r+2} + C_{2r-2}] + F_{2r}[C_{2r+2n} + C_{2r-2n}] = 0,$$

where $D_{2r} = [q_x/(2r + \beta_x)^2 - a_x b_1^2]$ and $F_{2r} = [p_x/(2r + \beta_x)^2 - a_x + b_1^2]$.

of damping) by the isosurfaces at integer values of βx in the three-dimensional parameter space spanned by (a_x ; q_x ; p_x).

A slice in the $a_x = 0$ plane (that is, when no DC offset is applied to the trap electrodes) for different values of the frequency ratio $n = \Omega_2 / \Omega_1$ is depicted in Fig. (2.7). The βx parameter was evaluated with the code found in Appendix (A). Fig. (2.7) shows how the fast frequency Ω_2 induces $n - 1$ tongues of subharmonic resonances that cut the stability zone down to the $q = 0$ axis.

For high values of n , these instabilities become denser and narrower. However, the finite resolution of the numeric code acts as an effective damping limiting the visibility of the resonances near the horizontal axis.

The motional instabilities inside a Paul trap arising from parametric resonances induced by a second frequency have been studied in various experimental and theoretical works. Recently, the two-frequency scheme was applied to the completely different task of stably trapping two ion species with a very large difference in their charge-to-mass ratios. This theoretical proposal is gaining the attention of experimental groups that work with multiple ion species or larger charged objects in a Paul trap. The following section will provide a basic theoretical treatment for our case of interest: trapping a calcium ion together with a charged silica nanosphere.

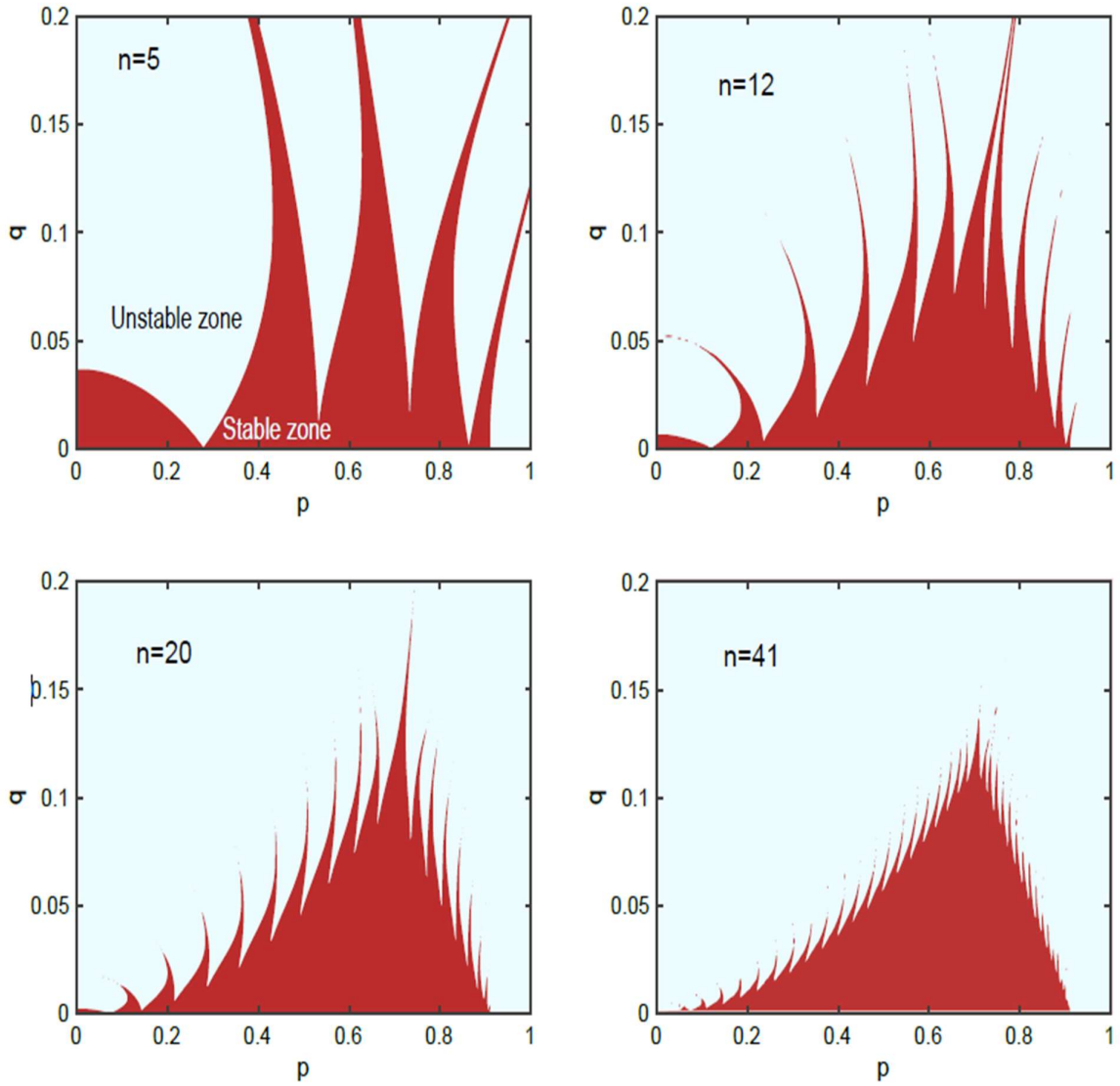


FIGURE 3.2: Stability diagrams for a two-frequency-driven Paul trap along the $a = 0$ plane. At a fixed operating frequencies, p is proportional to the strength of the field oscillating at the fast frequency ω_2 while q is proportional to the strength of the field oscillating at the slow frequency $\omega_1 = \omega_2 / n$. The slow field induced $n - 1$ parametric resonances which makes the trap unstable. The width of instability exponentially decreases in reaching the $q = 0$ axis, making them difficult to resolve.

3.4 BASIC TRAP DYNAMICS

3.4.1 A UNIFORM FIELD EXAMPLE

Consider a charged particle placed inside an ideal parallel-plate capacitor, as shown schematically in Figure. Assume that the plates are large and separated by a distance d , and there is a vacuum between the plates. As long as the fields do not change too rapidly, we can

assume a uniform electric field in the space between the plates, at any time equal to $\mathbf{E}(t) = \mathbf{V}(t)/\mathbf{d}$, where $V(t)$ is the applied voltage. Assume a sinusoidally oscillating voltage, $\mathbf{V}(t) = V_0 \cos \omega t$ which gives an electric field between the plates $\mathbf{E}(t) = E_0 \cos \omega t$ with $E_0 = V_0/d$. In this field we place a particle having a charge q , as shown in Figure 3.3.

The time-dependent electric force on the particle is

$$\mathbf{F}(t) = q\mathbf{E}(t) = qE_0 \cos \omega t$$

so the motion of the particle in the z direction is described by the equation of motion ($F = ma$).

$$m\ddot{z} = qE_0 \cos \omega t$$

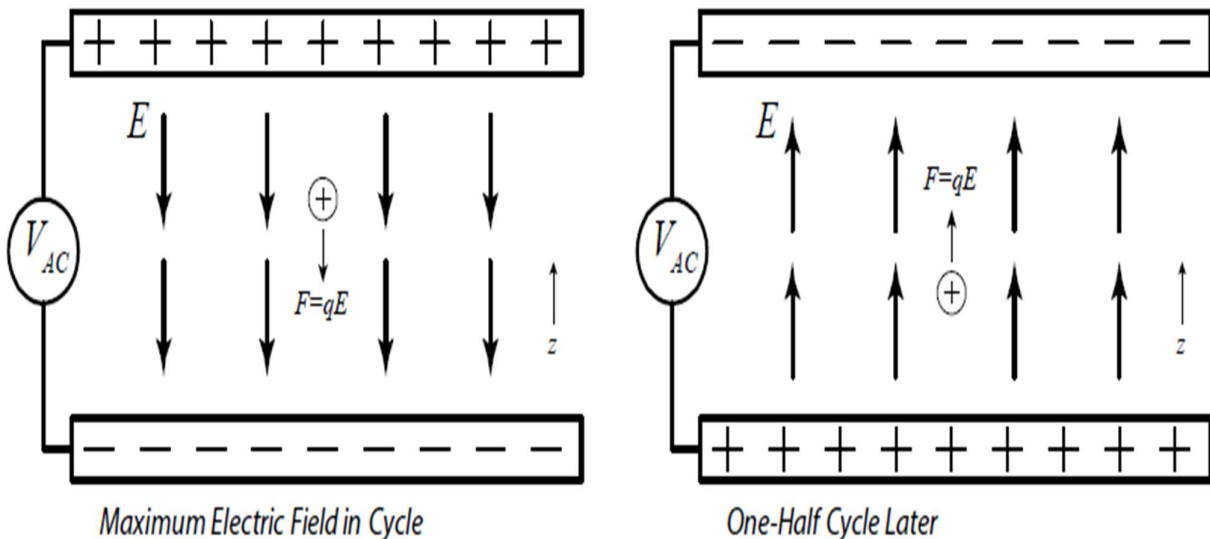


FIGURE 3.3. A charged particle placed initially at rest inside a parallel-plate capacitor. An oscillating voltage is applied to the capacitor, so the electric field oscillates with time. At any given time, however, the field is uniform between the plates. The oscillating electric field causes the particle position to oscillate. When the particle position is high (left), the electric field pushes it down. When the particle is low (right), the electric field pushes it back up. The average particle position (z) remains constant.

To solve this equation, we try a solution of the form

$$z = A \cos \omega t, \text{ giving}$$

$$\dot{z} = -\omega A \sin \omega t$$

$$\ddot{z} = -\omega^2 A \cos \omega t$$

and this gives the full solution

$$\begin{aligned} -m\omega^2 A \cos \omega t &= qE_0 \cos \omega t \\ \implies A &= -\frac{qE_0}{m\omega^2} \end{aligned}$$

where z_{init} is the initial position of the particle and v_{init} is its initial velocity. Note that this solution works in various trivial limits, for example if $q = 0$.

$$z(t) = z_{\text{init}} + v_{\text{init}}t - \frac{qE_0}{m\omega^2} \cos \omega t$$

[Note also that you can easily prove to yourself that Equation satisfies the equation of motion – just plug the solution into the equation and see that it works. Proving that Equation is the only possible solution is not so simple.

Uniqueness Theorems doing just that are the subject of advanced courses in differential equations. If we take $v_{\text{init}} = 0$ just to make life simpler, then the solution becomes

$$\begin{aligned} z(t) &= z_{\text{init}} - \frac{qE_0}{m\omega^2} \cos \omega t \\ &= z_{\text{init}} + \Delta z(t) \end{aligned}$$

In other words, the particle stays where we initially placed it (see Figure 3.3), but the oscillating electric field causes the particle position to oscillate. We will call $\Delta z(t)$ the particle micromotion, since we will typically assume this motion is fast and small. Motion over times much longer than $T = 1/\omega$ is often called the **secular motion**.

Since the particle position is 180 degrees out of phase with the applied force: when Δz is positive, the force is negative, so the force pushes the particle back toward z_{init} . When Δz is negative, the force is positive, so again the force pushes the particle back toward z_{init} . This behavior is shown in Figure 3.3. So in this simple example the particle just oscillates about z_{init} .

3.4.2 ADD AN ELECTRIC FIELD GRADIENT

After adding a field gradient, the electric field is no longer uniform in space. One way to add an electric field gradient is to curve the plates of our capacitor a bit, as shown in Figure 3.4.

For example, the two plates in the figure might be sections of spherical shells, where the geometrical centers are both located at the same point high above the plates.

The details of the plate geometries are not especially important. What is important is that the electric field lines look roughly like those shown in Figure 3.4 – in particular, the field strength

near the top plate is higher than near the bottom plate (note the lengths of the field vectors in the Figure.) Since we only curved the plates slightly, we haven't changed the field much, so the particle micromotion is about the same as it was before – the particle essentially just oscillates about its initial position.

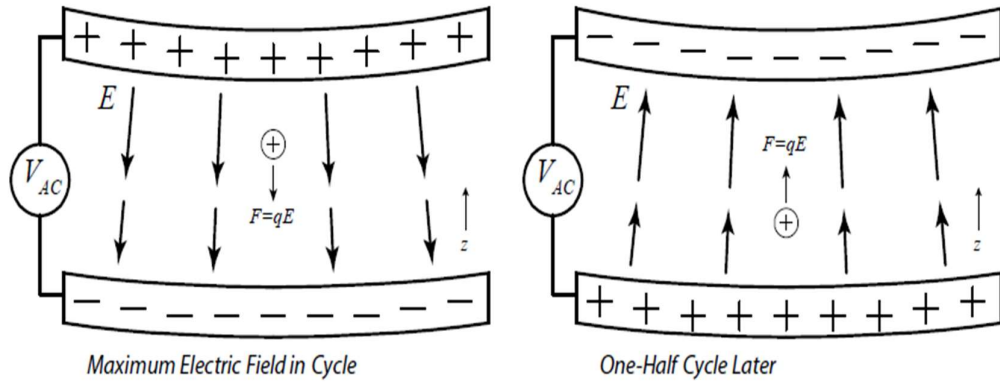


FIGURE 3.4. A charged particle placed initially at rest inside a curved-plate capacitor. The geometry of the plates causes a gradient in the electric field strength - the field is stronger for larger (as shown by the longer arrows). The imbalance means that the electric force on the particle is stronger at the top of its motion (left) and weaker at the bottom (right). Averaging over time, there is a net force that pushes the particle down, toward the weaker-field region.

But now we can see, just from the geometry in Figure 3.4, that the force over one cycle no longer averages to zero. As shown in the Figure, when Δ is positive (left side of the figure), the particle experiences a stronger-than-average electric field pushing it downward. And when Δ is negative (right side of the figure), the upward force is weaker than average. This imbalance was not present in Figure 3.3. From this fairly basic reasoning, shown graphically in Figure 3.4, we deduce that there is a net force pushing the particle down. Put another way, the secular force, averaged over many oscillation cycles, pushes the particle toward a region where the oscillating electric field is weaker.

The math all supports this, as we can demonstrate. We write the modified field as where $E' = dE/dz$. We assume that E' is small, so the particle micromotion is not much

$$E(z, t) = (E_0 + E' z) \cos \omega t$$

different from the $E' = 0$ case. Here we also assume that we are initially placing the particle at $z_{\text{init}} = 0$ which is halfway between the plates, just to simplify the equations.

With the added field gradient, the equation of motion becomes

$$m\ddot{z} = q(E_0 + E'z) \cos \omega t$$

Solving this exactly is nontrivial, but we can capture the essence of physics by looking at the limit of low E' . Setting $E' = 0$ gives the micromotion we saw previously

$$z(t; E' = 0) = -\frac{qE_0}{m\omega^2} \cos \omega t$$

and for small E' we assume that the micromotion shouldn't change much. We use this to calculate an average force on the particle as follows.

The total force on the particle at any given time is

$$F = q(E_0 + E'z) \cos \omega t$$

and we write the average force.

$$\langle F \rangle = \langle q(E_0 + E'z) \cos \omega t \rangle$$

where the average is over one oscillation cycle. Since E_0 is constant, we see that

$$\langle qE_0 \cos \omega t \rangle = qE_0 \langle \cos \omega t \rangle = 0$$

$$\langle F \rangle = \langle qE'z \cos \omega t \rangle$$

Into this we substitute in the $z(t; E' = 0)$ solution to give an approximate answer. While this is certainly not an exact result, we can expect that it may be reasonably accurate in the limit of

$$\begin{aligned} \langle F \rangle &\approx \left\langle qE' \left(-\frac{qE_0}{m\omega^2} \cos \omega t \right) \cos \omega t \right\rangle \\ &\approx -\frac{q^2 E' E_0}{m\omega^2} \langle \cos^2 \omega t \rangle \end{aligned}$$

low E' .

Since

$$\langle \cos^2 \omega t \rangle = \frac{1}{2} (\sin^2 \omega t + \cos^2 \omega t) = \frac{1}{2},$$

we can write,

$$\langle F \rangle \approx -\frac{q^2 E' E_0}{2m\omega^2}$$

So finally the negative sign in this expression means that $\langle F \rangle$ pushes the particle toward a region of weaker electric fields. Numerically integrating the equation of motion would give more accurate results, but this equation is a good first step, and it is sufficient for the present discussion. We see that the math confirms our simple reasoning above, and the equation gives a reasonable quantitative approximation for the secular force.

Several key conclusions can be drawn from this discussion: 1) The particle motion separates into two regimes, the micromotion that occurs on timescales comparable to the oscillation period, and the secular motion that occurs on timescales long compared to the oscillation period; 2) the secular force is reasonably well approximated by Equation; and 3) the secular force pushes particles toward regions of weaker oscillating fields.

The last point turns out to be remarkably general, and this is an important fact. For any slowly-varying, physically reasonable field geometry, the secular force always pushes particles toward regions of weaker oscillating fields. We showed this for a special case above; the general case is more difficult to prove.

One very convenient way to think about all this is with a trap pseudopotential $U_{\text{trap}} = (\text{KE})_{\text{micromotion}}$. Here the trap pseudopotential U_{trap} is simply equal to the kinetic energy of the particle micromotion. And the secular force is then equal to the gradient of U_{trap} .

3.5 QUADRUPOLE TRAPS

One easy way to make a 3D quadrupole trap is shown in Figure 3.5. An AC voltage is applied to two ball-shaped electrodes in a grounded box, creating oscillatory electric fields inside the box. Halfway between the balls, the electric field is always zero by symmetry. Near this zero-field point, the electric fields at one point in the AC cycle are shown in the Figure. Multiply these vectors by $\cos(\omega t)$ to obtain the electric fields at other times.

With this field geometry we see that the electric field strength increases in all directions outward from the zero field point halfway between the balls. Thus has a minimum at the zero-

field point, since the particle micromotion increases in all directions out from that point. Thus the secular forces will push particles toward the zero-field point, trapping them there.

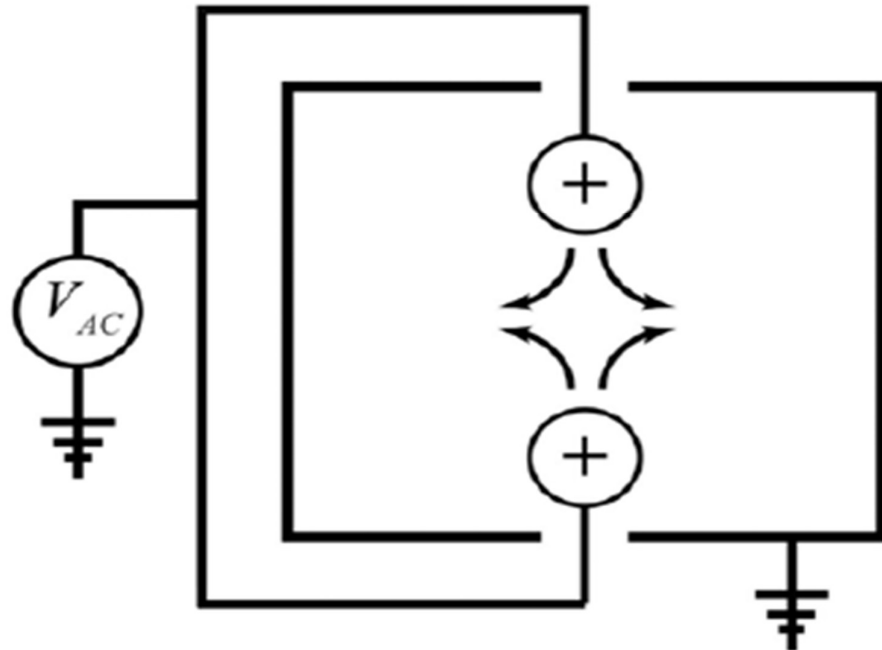


FIGURE 3.5. One method for making a 3D quadrupole ion trap, using two ball electrodes in a grounded box. When the balls are at a high potential relative to the box, the electric field lines are shown roughly by the arrows. Note by symmetry the electric field halfway between the balls is always zero.

Another approach for making a 3D quadrupole trap is the Ring Trap shown in Figure 3.6. Again the electric field at the center of the ring is always zero, and the arrows show the fields in the vicinity of this central region at one point in the cycle.

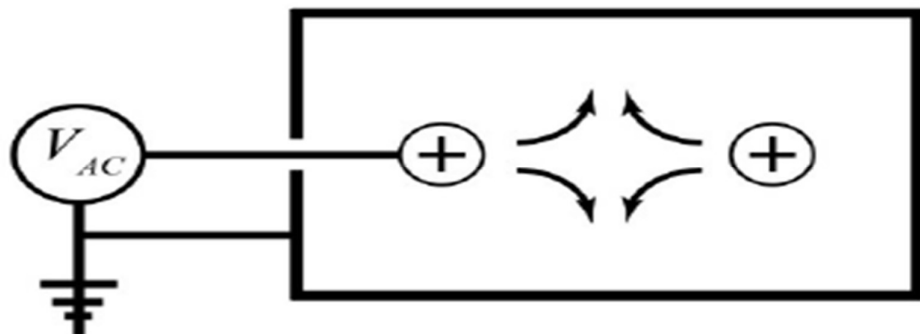


FIGURE 3.6. Another method for making a 3D quadrupole trap, which is essentially the geometry used in the Ring Trap, one of three ion traps that are part of the EIT instrument. In this configuration a ring electrode (seen edge-on here) is inside a grounded box, and the potential between the two is set by an applied AC voltage.

Both these examples show electric field geometries that: 1) have zero electric field at a center point, 2) have field magnitudes that increase in all directions away from the central point, and 3) exhibit axial symmetry. We can quantify this picture of quadrupole geometries by looking at the fields near the zero-field regions. Around the center points we can do a multipole expansion of the fields, which is essentially a Taylor series expansion of the vector fields (a bit more complicated than a Taylor expansion of a 1D function, but it's the same principle.) Doing this (given without proof here) reveals that the electric potential can be approximated near the trap center ($r = z = 0$) as

$$V(r, z)_{\text{3D-Quad}} = A_0 + A_2 [2z^2 - r^2] \cos \omega t$$

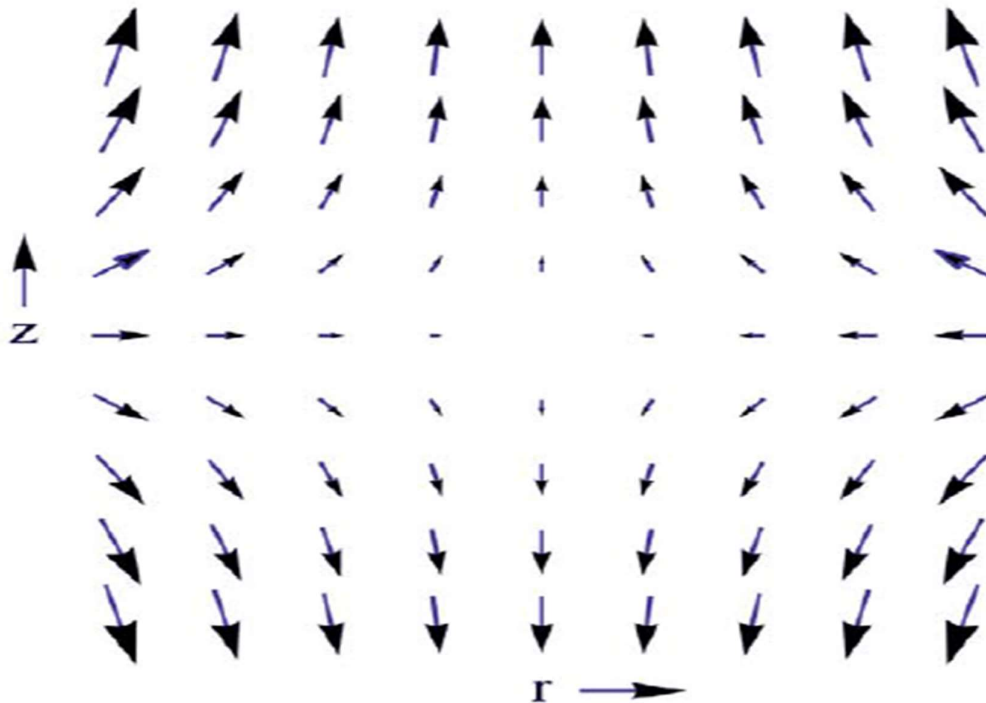


FIGURE 3.7. The 3D quadrupole electric field geometry near the center of the Ring Trap and the Single Particle Trap. This shows the electric field vectors when the ring voltage is at its maximum. Multiply each vector by $\cos(\omega t)$ to obtain the electric fields at other times.

where A_0 and A_2 are constants. The electric fields are then

$$\begin{aligned} E_z &= -\frac{\partial V}{\partial z} = -4A_2 z \cos \omega t \\ E_r &= -\frac{\partial V}{\partial r} = 2A_2 r \cos \omega t \end{aligned}$$

and a vector plot is shown in Figure 3.7. Note that the electric field strength increases linearly with r and z as one goes out from the origin.

If we do this for the 2D case, then we find (again given without proof here) that the electric potential can be approximated near the trap center ($x = y = 0$) as

$$V(x, y)_{\text{2D-Quad}} = A_0 + A_2 [x^2 - y^2] \cos \omega t$$

where A_0 and A_2 are constants. From this we can calculate the electric fields

$$\begin{aligned} E_x &= -\frac{\partial V}{\partial x} = -2A_2 x \cos \omega t \\ E_y &= -\frac{\partial V}{\partial y} = 2A_2 y \cos \omega t \end{aligned}$$

and a vector plot of these fields is shown in Figure 3.8. Again we see that the electric field strength increases linearly with x and y near the origin.

At this point it is beneficial to pause, stare at the electric field plots for a while, and ponder what is going on inside these traps. At the trap center, there are no electric fields, so no electric forces at all. A particle at the trap center, with no velocity, would just sit there. Away from the trap center, the electric fields are nonzero, so a charged particle experiences what we are calling the micromotion – it oscillates back and forth, in our case at 60 Hz. Averaging over a few cycles, there is also a weaker secular force that pushes the particles toward the origin. All around the origin, in any direction, the particles are pushed toward the origin. Thus charged particles become trapped at the origin.

Key in this discussion is to separate in your head the micromotion from the secular motion. The micromotion exists whenever the oscillating fields are nonzero.

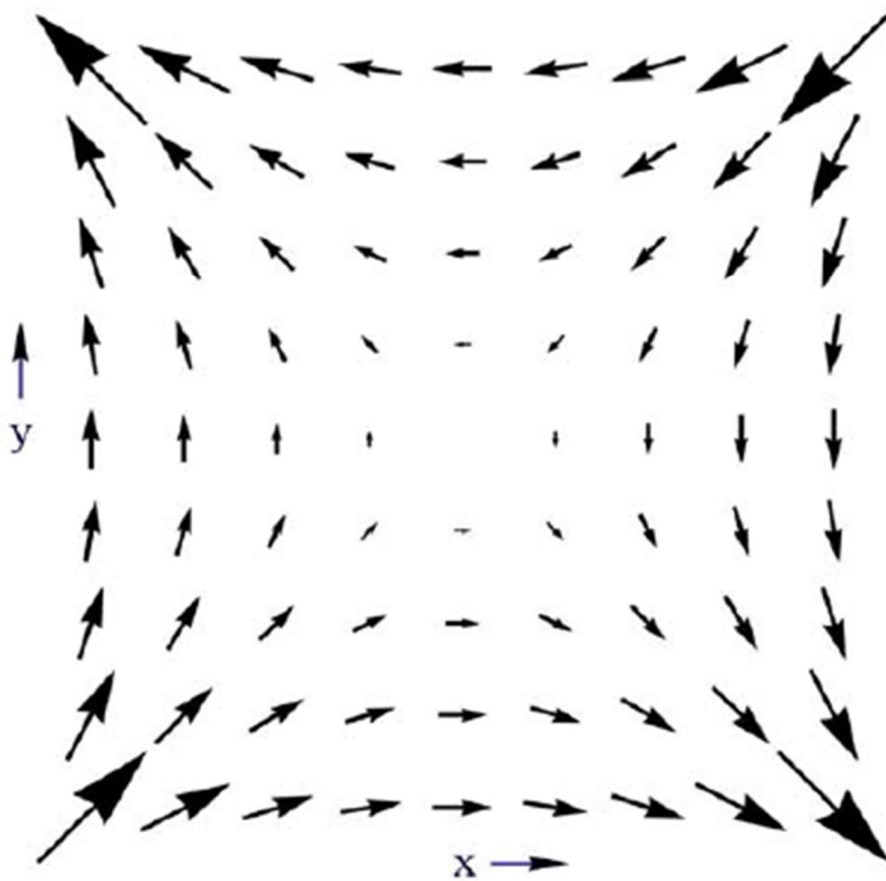


FIGURE 3.8. The 2D quadrupole electric field geometry near the center of the Linear Trap. This shows the electric field vectors when the applied voltage is at its maximum. Multiply each vector by $\cos(\omega t)$ to obtain the electric fields at other times.

But you can average over the micromotion and extract the average secular force (F), as we did above. All the stationary forces, such as gravity, combine with (F) to determine the long-term behavior of the particle. The pseudopotential Utrap is especially useful for visualizing the secular forces.

3.6 THE TRIBOELECTRIC SERIES

Most Positive (+)	
Air	
Human Hands, Skin	
Asbestos	
Rabbit Fur	+++
Glass	
Human Hair	
Mica	
Nylon	←
Wool	
Lead	
Cat Fur	+
Silk	
Aluminum	
Paper	
Cotton	
Steel	
Wood	
Lucite	
Sealing Wax	-
Amber	
Rubber Balloon	
Hard Rubber	
Mylar	
Nickel	
Copper	
Silver	
uv Resist	
Brass	
Synthetic Rubber	
Gold, Platinum	
Sulfur	
Acetate, Rayon	
Polyester	
Celluloid	
Polystyrene	
Orlon, Acrylic	
Cellophane Tape	
Polyvinylidene chloride (Saran)	
Polyurethane	
Polyethylene	
Polypropylene	
Polyvinylchloride (Vinyl)	
Kel-F (PCTFE)	
Silicon	
Teflon	←
Silicone Rubber	
Most Negative (-)	

FIGURE 3.9. A diagram showing the Triboelectric Series, adapted from http://www.siliconfareast.com/tribo_series.htm. Materials near the top tend to become positively charged when rubbed, while those near the bottom become negatively charged. In the Electrodynamic Ion Traps apparatus we use Teflon and Nylon “wands” to pick up, charge, and deliver particles for trapping.

3.7 DAMPED ION TRAPS

Going back to the parallel plate capacitor example shown in Figure 3.3, the electric force remains $F = qE = qE_0 \cos \omega t$, and to this we add viscous damping $F = -\gamma v$ where γ is the usual damping constant and $v = \dot{z}$ is the particle velocity. The equation of motion then becomes where $\Gamma = \gamma/m$. This time we write the equation in its complex form

$$\begin{aligned} m\ddot{z} &= qE_0 \cos \omega t - \gamma \dot{z} \\ \ddot{z} + \Gamma \dot{z} &= \frac{qE_0}{m} \cos \omega t \\ -\omega^2 A e^{i\omega t} + i\omega \Gamma A e^{i\omega t} &= \frac{qE_0}{m} e^{i\omega t} \\ A &= -\frac{qE_0/m}{\omega^2 - i\omega\Gamma} \end{aligned}$$

and the final solution (assuming $v_{\text{init}} = 0$) is given by the real part of the complex solution, giving

$$\begin{aligned} z(t) &= z_{\text{init}} - \text{Re} \left[\frac{qE_0/m}{\omega^2 - i\omega\Gamma} e^{i\omega t} \right] \\ &= z_{\text{init}} + \Delta z(t) \end{aligned}$$

Note that if we assume $\Gamma = 0$ (no damping), then we recover the solution above, in Equation 2. If $\Gamma = 0$ then note that the amplitude of the oscillatory term is always smaller than what we found above. This makes sense; we would expect the addition of damping to reduce the amplitude of driven oscillations.

Carrying the math a bit further, we have

$$\begin{aligned}
\Delta z(t) &= -\operatorname{Re} \left[\frac{qE_0/m}{\omega^2 - i\omega\Gamma} e^{i\omega t} \right] \\
&= -\operatorname{Re} \left[\frac{qE_0/m}{\omega^2 - i\omega\Gamma} \frac{\omega^2 + i\omega\Gamma}{\omega^2 + i\omega\Gamma} e^{i\omega t} \right] \\
&= -\frac{qE_0/m}{\omega^4 + \omega^2\Gamma^2} \operatorname{Re} [(\omega^2 + i\omega\Gamma)(\cos \omega t + i \sin \omega t)] \\
&= -\frac{qE_0}{m} \frac{1}{\omega^4 + \omega^2\Gamma^2} [\omega^2 \cos \omega t - \omega\Gamma \sin \omega t] \\
&= -\frac{qE_0}{m} \frac{1}{\omega^2 + \Gamma^2} \left[\cos \omega t - \frac{\Gamma}{\omega} \sin \omega t \right]
\end{aligned}$$

And again we note that this reduces to Equation 2 when $\Gamma = 0$ as we would expect.

We now compute the trapping force by averaging over one cycle, as we did above. The force on the particle at any given time is

$$F = q(E_0 + E'z) \cos \omega t$$

and the average force becomes (see above)

$$\begin{aligned}
\langle F \rangle &= \langle qE'z \cos \omega t \rangle \\
\langle F \rangle &\approx \left\langle qE' \left(-\frac{qE_0}{m} \frac{1}{\omega^2 + \Gamma^2} \cos \omega t \right) \cos \omega t \right\rangle \cos \omega t \\
&\approx -\frac{q^2 E' E_0}{m} \frac{1}{\omega^2 + \Gamma^2} \langle \cos^2 \omega t \rangle \\
&\approx -\frac{q^2 E' E_0}{2m} \frac{1}{\omega^2 + \Gamma^2}
\end{aligned}$$

Since $\langle \sin \omega t \cos \omega t \rangle = 0$ this becomes

Comparing this with Equation 3, we see that damping reduces $\langle F \rangle$ compared to the $\Gamma = 0$ case, which again seems intuitively plausible.

3.7.1 STOKES DAMPING

To calculate the damping constant, we start with the Reynolds number

$$\operatorname{Re} \approx \rho v R / \eta$$

where ρ is the fluid density, v is the particle velocity, R is the particle radius, and η is the dynamical viscosity. For our trapped particles in air, $v \approx 1 \text{ mm}/(1/60 \text{ sec}) \approx 6 \text{ cm/sec}$, $R \approx 10 \text{ m}$, and for air at a pressure of one atmosphere

we have $\rho \approx 12 \text{ kg/m}^3$ and

(26)

$$\eta = 1.8 \times 10^{-5} \text{ kg/m-s}$$

so $Re \approx 0.04$

For such a low Reynolds number, the air damping is well approximated by Stokes damping, given by

$$F = -6\pi\mu Rv$$

and we see that the force is proportional to $-v$ which is typical of a friction force. This gives a damping constant

$$\gamma = 6\pi\mu R$$

$$\begin{aligned}\Gamma &= \frac{\gamma}{m} \\ &= \frac{6\pi\mu R}{\frac{4}{3}\pi R^3 \rho_{part}} \\ &= \frac{9}{2} \frac{\mu}{R^2 \rho_{part}}\end{aligned}$$

where ρ_{part} is the particle density.

Assuming a density of $\rho_{part} \approx 500 \text{ kg/m}^3$, and using the other parameters above, this gives

$$\Gamma \approx 1620 \text{ s}^{-1}$$

which is substantially larger than $w = 2\pi(60 \text{ Hz}) = 377 \text{ s}^{-1}$. For example, the secular trapping force in Equation 6 becomes

$$\langle F \rangle \approx -\frac{q^2 E' E_0}{2m\Gamma^2}$$

to an accuracy of about five percent.

With this “overdamped” approximation, the micromotion becomes

$$\begin{aligned}E(t) &= E_0 \cos \omega t \\ \Delta z(t) &= -\operatorname{Re} \left[\frac{qE_0/m}{\omega^2 - i\omega\Gamma} e^{i\omega t} \right] \\ &\approx \operatorname{Re} \left[\frac{qE_0/m}{i\omega\Gamma} e^{i\omega t} \right] \\ &\approx \frac{qE_0}{m\omega\Gamma} \sin \omega t\end{aligned}$$

(27)

In the overdamped limit, the motion is 90 degrees out of phase with the drive force, rather than 180 degrees out of phase, as we saw above.

3.7.2 PARTICLE DYNAMICS IN A QUADRUPOLE TRAP

Next consider a particle in a 3D quadrupole trap, and look at the motion. From Equation 4, the oscillatory electric field is

$$\begin{aligned} E_z &= -4A_2 z \cos \omega t \\ &= E_0(z) \cos \omega t \end{aligned}$$

so $E_0(z) = -4A_2 z$ where A_2 depends on the applied voltage and the geometry of the trap. For convenience we can write

$$E_0(z) = \frac{V_{AC}}{z_{\text{eff}}} z$$

where z_{eff} is a constant that depends on the geometry of the trap, and we expect z_{eff} to be comparable to the spacing between the trap electrodes. This replaces one constant (A_2) with another, more physically defined, constant (A_2) with another more physically defined constant (z_{eff}).

We are also free to define the sign of V_{AC} to remove the minus sign from the expression. Changing the constants in this way simply makes the subsequent math a bit simpler and more intuitive.

The field gradient is

$$\begin{aligned} E'(z) &= \frac{dE_0(z)}{dz} \\ &= \frac{V_{AC}}{z_{\text{eff}}^2} \end{aligned}$$

The trapping force is then

$$\begin{aligned} \langle F \rangle &\approx -\frac{q^2 E' E_0}{2m} \frac{1}{\omega^2 + \Gamma^2} \\ &\quad -\frac{q^2}{2m} \left(\frac{V_{AC}}{z_{\text{eff}}^2} \right)^2 \frac{1}{\omega^2 + \Gamma^2} z \\ &\approx -\frac{q^2 V_{AC}^2}{2m z_{\text{eff}}^4} \frac{1}{\omega^2 + \Gamma^2} z \\ &\approx -\frac{q^2 V_{AC}^2}{2m z_{\text{eff}}^4 \Gamma^2} z \end{aligned}$$

(28)

using overdamped approximation, which is accurate to about 4 percent.

Apply an external force F_{ext} , then the particle will settle to an equilibrium position z_{eq} where the trapping force $\langle F \rangle$ balances the external force F_{ext} , giving

If we let $F_{ext} = qE_{static} - mg$, then

$$\begin{aligned}\frac{q^2 V_{AC}^2}{2mz_{eff}^4 \Gamma^2} z_{eq} &\approx F_{ext} \\ z_{eq} &\approx \frac{2mz_{eff}^4 \Gamma^2}{q^2 V_{AC}^2} F_{ext} \\ z_{eq} &\approx \frac{2mz_{eff}^4 \Gamma^2}{q^2 V_{AC}^2} (qE_{static} - mg) \\ &\approx \frac{2mz_{eff}^4 \Gamma^2}{qV_{AC}^2} \Delta E_{static} \\ \Delta E_{static} &= E_{static} - \frac{mg}{q}\end{aligned}$$

Balancing gravity gives us a measurement of q/m and z_{eff} is derived from the trap geometry. Thus a measurement of the slope of $z_{eff}(\Delta E_{static})$ gives direct measure of Γ and from this the particle radius R can be independently determined.

Also measure micromotion under application of ΔE_{static}

$$\Delta z(t) = -\frac{qE_0}{m} \frac{1}{\omega^2 + \Gamma^2} \left[\cos \omega t - \frac{\Gamma}{\omega} \sin \omega t \right]$$

Amplitude of oscillation in overdamped approximation ($\Gamma \gg \omega$)

$$\begin{aligned}\Delta z_{max} &\approx \frac{qE_0}{m} \frac{1}{\omega^2 + \Gamma^2} \frac{\Gamma}{\omega} \\ &\approx \frac{qE_0}{m} \frac{1}{\omega \Gamma} \\ &\approx \frac{q}{m} \frac{1}{\omega \Gamma} \frac{V_{AC}}{z_{eff}^2} z_{eq} \\ &\approx \frac{q}{m} \frac{1}{\omega \Gamma} \frac{V_{AC}}{z_{eff}^2} \frac{2mz_{eff}^4 \Gamma^2}{qV_{AC}^2} \Delta E_{static} \\ &\approx \frac{2z_{eff}^2 \Gamma}{\omega V_{AC}} \Delta E_{static}\end{aligned}$$

(29)

$$\frac{q}{m} \frac{1}{\omega \Gamma} \frac{V_{AC}}{z_{eff}^2} = 1$$

so again measure Γ

Unstable orbit when $\Delta z_{max} = z_{eq}$ which from the above means

$$V_{AC} < \frac{m\omega\Gamma z_{eff}^2}{q}$$

so stability requires

and once again we measure Γ .

CHAPTER 4

EXPERIMENTAL APPARATUS

4.1 THE LINEAR TRAP REALIZATION

4.1.1 DESIGN AND FABRICATION

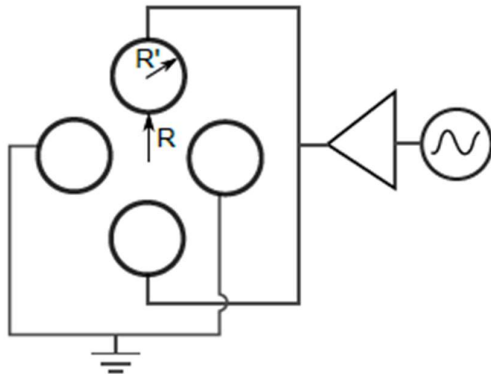


FIGURE 4.1: Section view of the four rod Paul trap. Two diametrically opposed cylindrical electrodes (with radius R_0 separated by a distance $2R$) are connected to the RF source, while the remaining two are grounded through the optical table.

In Fig. (4.1) The general idea of the trap is sketched based on a simple quadrupole mass filter: two dielectric holders support four cylindrical electrodes for radial confinement and two additional smaller rods placed as end caps for axial confinement.

Three additional rods are included, to which DC voltages can be applied in order to compensate for stray electric fields that can displace the particle from the RF minimum, causing excess micromotion. These rods are known as compensation electrodes.

4.1.1.1 HOLDERS

All of the trap electrodes are fitted in the dielectric holders, which are the only parts that required custom design and fabrication.

The holder is a dielectric slab with holes that match the electrodes' diameters. It keeps the electrodes parallel while ensuring the stability of the trap and providing a clamping mechanism for the system. The design of the holder is shown in Fig. (4.2). Given the fixed radius of the rods (R'), the separation of the electrodes (R) was chosen as shown in Fig (4.1)

$$R' = 1.03R$$

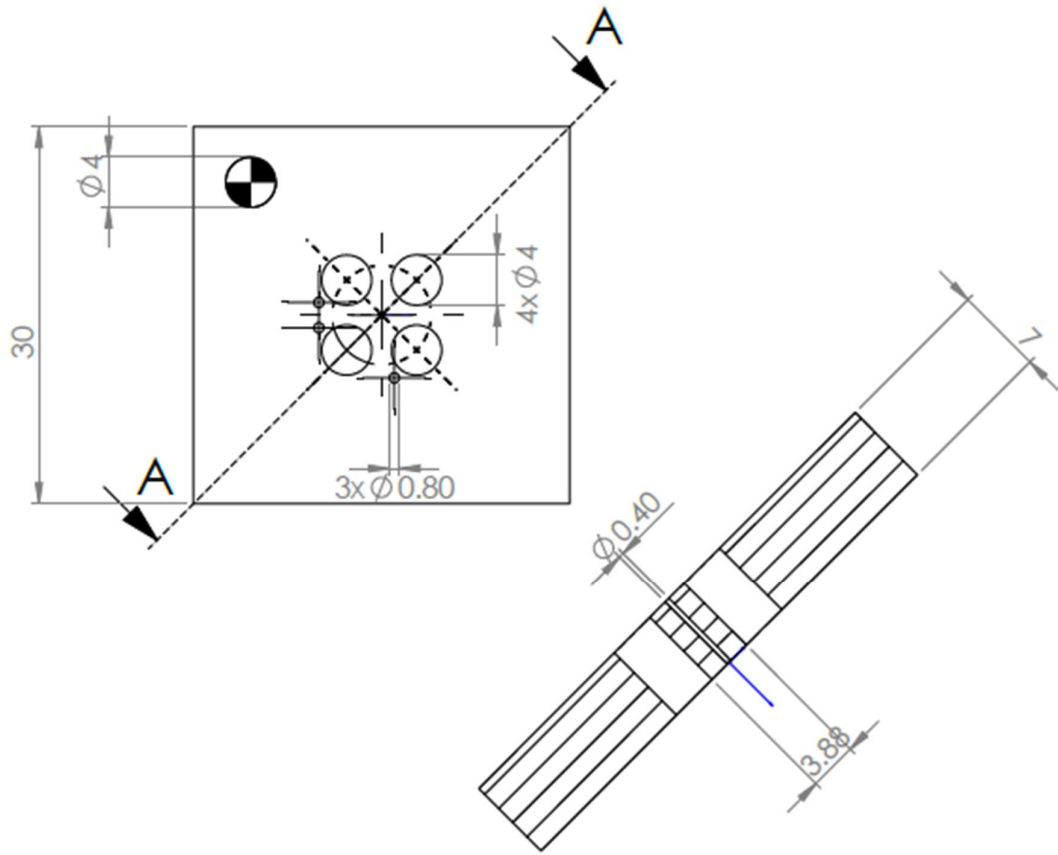


FIGURE 4.2: CAD drawing of one of the two identical holders for the Paul trap. All lengths are expressed in mm. The holes are: four 4mm diameter holes for RF/ground electrodes; one 0.4mm diameter center hole for the endcap electrode; two M4 threaded holes to accommodate screw connections with a post; three additional 0.8mm diameter holes for compensation electrodes.

The electric field profile arising from this geometrical arrangement of electrodes has been studied through finite element simulations. For these simulations, the pseudopotential $\square_{pseudo}(x, y)$ can be written as

$$\varphi_{pseudo}(x, y) = \frac{Q}{4m\Omega_{drive}^2} |E(x, y)|^2$$

where Q and m are respectively the charge and the mass of the trapped particle and \square_{drive} is the drive frequency of the trap. The confining potential will be harmonic only within the region where the square of the electric field depends quadratically on the radial coordinates x and y. This occurs for distances from the center of the trap less than 0.4 mm, as determined from the simulations shown in Fig. (4.3).

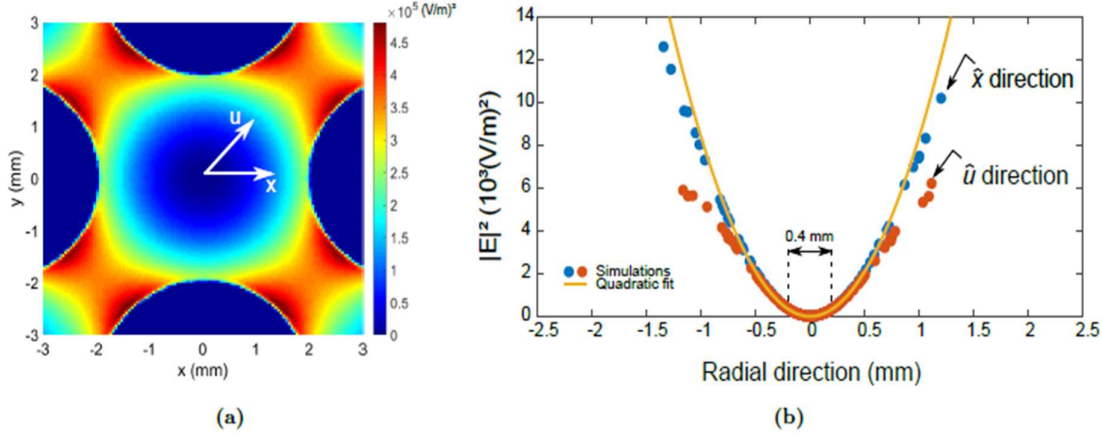


FIGURE 4.3: Electrostatic simulations of E^2 arising from the geometrical configuration of eq., with 1V applied on the two RF rods. The resulting pseudopotential can be obtained with the help of Eq. Figure (a) shows a contour plot of E^2 on the $z=0$ plane. It can be seen how the radial symmetry manifests itself just near the center of the trap. Figure (b) shows that radial symmetry is achieved within a radius of 0.2mm from the center. Below that distance, a multipole expansion t showed that anharmonic terms became smaller than 1% of the quadratic term.

A ratio of $R'/R = 1.147$ would have led to a larger area of harmonicity of the trap. However, this would have implied a shorter distance between the cylindrical electrodes, compromising the fabrication process for the holder holes, and the optical access for imaging detection.

The holders have been fabricated with a precision of 0:02mm by the mechanical workshop of the University of Innsbruck's Institute for Experimental Physics.

The holders are made of polyoxymethylene (POM). POM is a polymer able to sustain up to 15 kVmm-1. DC fields before dielectric breakdown. We have never encountered breakdown problems while working between DC and 30 kHz and voltages applied to the rods (minimum separation of 1.5mm) up to 1 kV.

4.1.1.2 ELECTRODES

The electrodes were made from commercially available components.

The four RF electrodes (RF and ground, see Fig. (2.2)) are stainless steel assembly rods of a commercial cage system², 4mm in diameter and 50mm in length.

The endcap electrodes are dialysis needles made of stainless, chromium-nickel steel³, 0.4mm in diameter and 25mm in length. Three additional needles, 0.8mm in diameter and 120mm in length, were used as compensation electrodes.

4.1.1.3 POSITION OF ENDCAPS AND COMPENSATION ELECTRODES

The endcaps are placed in the center of the RF and ground electrode holes. In order to minimize the distortion of the quadrupole field potential, the compensation electrodes are smaller than the RF and ground rods and they are positioned further from the center.

4.1.1.4 TRAP ASSEMBLY

Fig. (4.4) shows the final form of the trap.

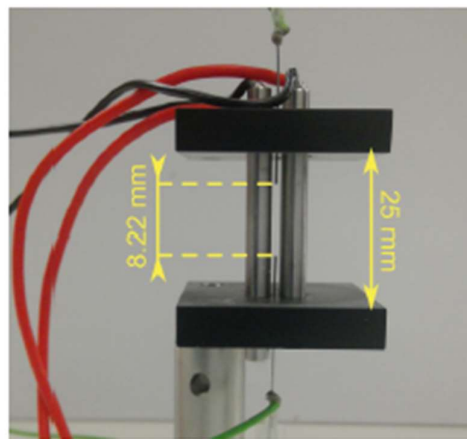


FIGURE 4.4: The trap assembled in vertical configuration. The bottom holder is clamped via an M4 screw to a post and is 25mm away from the top holder. The endcap separation is 8.22 mm.

An M4 threaded hole was machined on the holder in order to clamp the assembled trap to its mount and align the trap on the optical table using standard optomechanical components.

The electrodes are tightly fit into the holder by pressure, allowing the separation of the endcaps to be regulated manually. This also makes it easier to unmount and remount the trap for cleaning. After several particle loading sessions, in fact, the electrodes became dirty with the particle's solution (a detailed loading mechanisms description is given in Sec. 4.2).

Each electrode is connected to its power source via cables directly soldered onto it. The trap is mounted via a post to a one-axis translation stage that can be finely adjusted (see Fig. (4.5)) so that its lateral position with respect to the detection laser beam. An acrylic box covers the whole trap, protecting it from air flow.

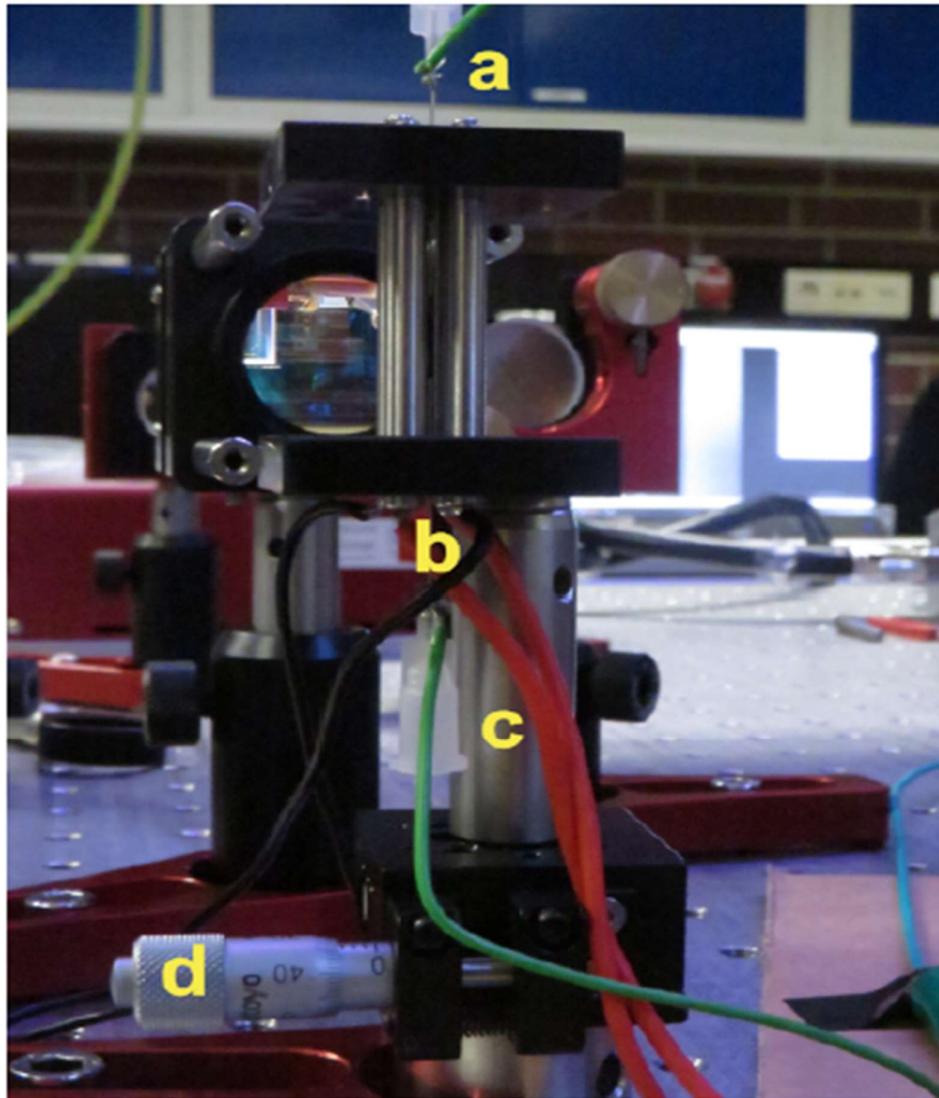


FIGURE 4.5: Trap mounted on the optical table. The electrical connections of the electrodes are a) for the top endcap (green wire) and b) for the bottom one (green wire) as well as the rods (red wires for the RF and black for GND). The bottom holder is fixed via an M4 screw to a post c), which is clamped to a linear translation stage d) for alignment of the trap with respect to the detection laser beam.

4.1.2 DRIVING THE TRAP

The Paul trap needs to be driven by a combination of AC and DC fields.

4.1.2.1 DC SOURCE

The endcaps and compensation electrodes are driven by DC fields. This static voltage is generated by a high precision HV module4 (Iseg box) which can provide up to 6 kV with low current (a fraction of a microampere).

4.1.2.2 AC SOURCE

As shown in Fig. (4.1), the RF rods across from one another are driven with the same AC voltage. The ground electrodes are grounded to the table.

The RF field is generated by an arbitrary waveform generator (AWG) and then amplified by a voltage amplifier. The AWG has two independent outputs that give a maximum of 5Vpp per channel when both are switched on and 10Vpp if just one is used.

The amplifier can reach a maximum amplitude of 1:4 kV DC or AC, with an output current range from 0 to 50 mA. The maximum output voltage depends on the capacitive coupling obtained with the trap. The gain of the amplifier is tunable with a knob up to 300. The input channel supports up to 20Vpp AC. To match the load impedance of the trap, the dynamic adjustment knob located on the front panel of the amplifier is used.

The output is monitored with a voltage divider that gives 1/200th of the output signal. A power splitter was used in order to feed the amplifier (which has just one input) with the sum of two RF fields, allowing us to investigate the behavior of the trap driven by two frequencies.

4.1.2.3 REMOTE CONTROL SYSTEM

Due to the number of control knobs in the experiment and the fact that high voltage is involved, it is useful to control the experiment hardware remotely. In our experiment, this is done with the Trapped Ion Control Software (TrICS).

TrICS is developed by the Quantum Optics and Spectroscopy Group of the University of Innsbruck, and allows users to control different hardware devices via their specific libraries or through an user API.

4.2 PARTICLE PREPARATION AND LOADING METHODS

The measurements reported here have been carried with two different sphere sizes. Hereafter we will refer to the largest ones ($21.8 \pm 0.9 \mu\text{m}$ from Micro particles GmbH) as microparticles, and to the smallest ones ($0.10 \pm 0.03 \mu\text{m}$ from Polysciences Inc.) as nanoparticles.

Both are stored as a solution (5% mass concentration) of nonporous SiO₂ in NaOH-enriched water. The stated densities are 1:85 g/cm³ for the microparticles and 2 g/cm³ for the nanoparticles. With these values, the average mass of a nanoparticle and of a microparticle are estimated to be around $1 \times 10^{-18} \text{ kg}$ and $1 \times 10^{-11} \text{ kg}$ respectively.

4.2.1 ELECTROSPRAY IONIZATION OF NANOPARTICLES

Electrospray ionization (ESI) is a technique used to obtain charged particles from a liquid solution. Fig. (4.6) depicts how ESI works. Solution is pumped through a metallic capillary needle, which is subjected to a high potential difference with respect to a counter electrode. The dissolved particles become charged via the triboelectric effect arising from the friction between the particles and both the walls and the polarized solvent.

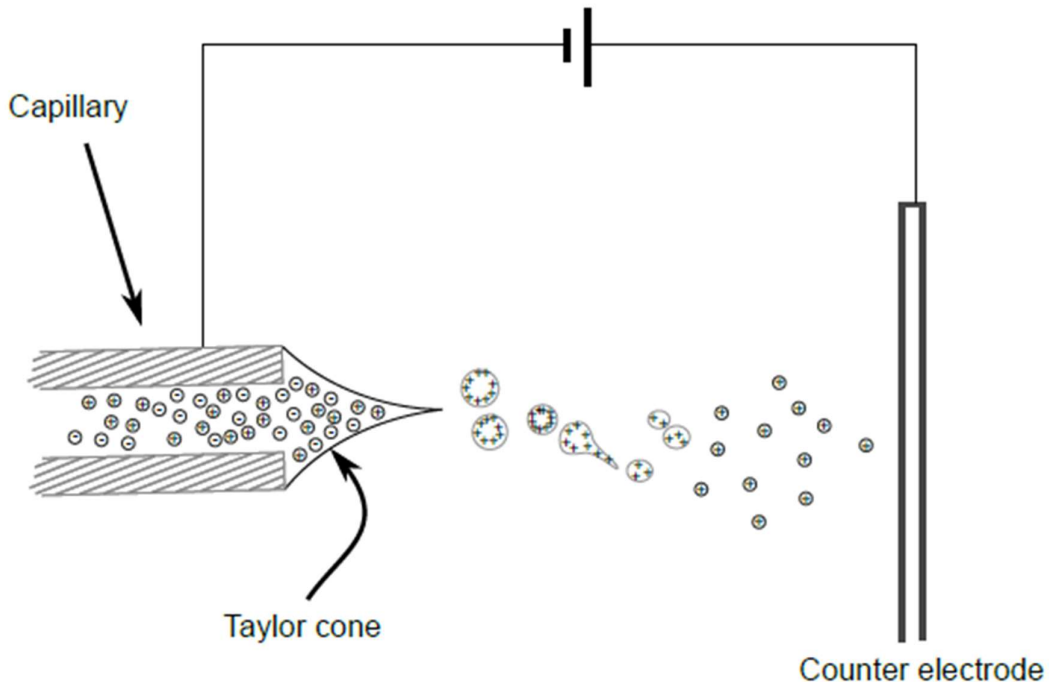


FIGURE 4.6: Electrospray working principle. A static voltage is applied between a capillary filled with the liquid solution and a counter electrode. When pressure is maintained on the plunger, the capillary will eject a spray of ionized particles grouped inside droplets of solvent. After the solvent has evaporated, the charged particles escape from the droplets, as they are accelerated by the electric field towards the counter electrode.

Once a certain threshold voltage is reached, the pressurized liquid exits from the needle and forms the so-called Taylor cone, named after the theoretical work of G. I. Taylor.

A spray of droplets is observed beyond the Taylor cone. These droplets are charged, and thus they are accelerated by the electric field toward the counter electrode. In the meanwhile, part of the solvent in the droplets evaporates. This leads to a decrease in the droplets' volume and a subsequent increase of surface charge density. When the electrostatic pressure exceeds the surface tension, the droplets break into smaller ones, with a cascade effect that stops with droplets containing a single charged nanoparticle.

Implementation in the Lab

A basic ESI system has been built for loading the nanospheres into the Paul trap. A medical syringe is fixed on a post and placed near the trap, pointing between the rods. The syringe's needle is connected via an alligator cable to the Iseg voltage source. The counter electrode is one of the two grounded rods of the trap itself. The syringe is filled with 10 μL of nanoparticle solution diluted with 0.5mL of ethanol (this is a quite standard trick, used to obtain a faster evaporation of the solvent). Applying little pressure by hand (enough to feed the small droplet at the tip of the syringe) and a voltage of 3 kV to the needle, a Taylor cone starts to appear. Illuminating the trapping region with a collimated laser beam ($= 650 \text{ nm}$), we can observe the trapped particles with naked eye (see Fig. (3.8)) and register their motion with a camera.

4.2.2 CHARGING AND LAUNCHING OF MICROPARTICLES

After several tests, we figured out that the method used for the nanospheres does not work with the microparticles. Therefore we decided to follow a different approach. A small volume of the microparticle solution diluted with ethanol is applied on a thin flat electrode connected to a Van de Graaff generator. The thin electrode is clamped on a post and placed close to the trap. Once switched on, the Van de Graaff generator produces a voltage difference of hundreds of volts by accumulating charges on the thin electrode. Some of these charges become attached to the surface of the dielectric spheres, which in turn are expelled from the electrode surface via electrostatic repulsion.

The difference between this method and the one used to charge the nanospheres is that the charging of microparticles is based only on the triboelectric effect, and does not involve evaporation of the solvent. Indeed, we are also trapped from a dry powder of microspheres initially deposited on the tip electrode, demonstrating that friction with the electrodes is sufficient to charge the particles.

It should be noted that the presence of residual ethanol in this case is unavoidable since the microparticle solution takes a long time to dry completely (approx 1 h). This turns out to be an advantage as it seems easier for the particles to become charged and expelled in a liquid emulsion than in a dry surface.

4.3 MATHEMATICAL BACKGROUND

Electrodes are strategically shaped and placed for desired electric field interactions. In our setup, the spherical brass balls are at the opposite potential of the ring electrode. The electric field then oscillates between two configurations at a frequency of 60 Hz, which is the frequency of the wall voltage. One of the configurations stretches the particles that are outside the center of the ring in the vertical direction and provides a restoring force towards the center in the horizontal direction, and the other configuration is the opposite, the particles are stretched horizontally, and there is a restoring force toward the center in the vertical direction. The rapid oscillation of the electric field between the two configurations provides an average conning force in all directions, because the trap field oscillates faster than the particles can escape the trap. Once particles settle into a place, they essentially oscillate in a fixed position very quickly. The oscillating and stretching in the horizontal and vertical directions causes the shape of the dust that we observe.

The electric potential within the device has been long studied and can be described by the equation

$$U = (U_0 + V_0 \cos wt) * (r^2 - 2(z^2)) / d^2$$

where 'w' is the radio frequency and $d = (1/2*(r^2) + z^2)^{1/2}$

Here, U_0 = Initial Voltage before setting up the device = 0 V

V_0 = Voltage applied to the system = 2000 V, w = frequency of ac input voltage = $2*3.14*50$ = $100*\pi$

r = radius of spherical electrodes = 2 cm = 0.02 metres, U (potential inside the system) = 3000 V (assumption);

Let z be the distance between electrodes;

Then, putting values in the above equation;

We find out; $z = 0.01$ metres (approx.) = 1 cm.

Hence distance between the two spherical electrodes of radius 2 cm is 1 cm.

The restoring force that drives the charged particle back toward the center of the device increases as the ion deviates from the center of the device. The motion of the charged particle in an ideal Paul trap is most commonly described by the solutions to the Mathieu equation:

$$\frac{d^2u}{dt^2} + (a - 2q \cos 2\tau) u$$

where u is the coordinate axes, T is a dimensionless parameter equaling to $t=2$, and a and q are additional dimensionless parameters known as trapping parameters. Mathieu functions appear in physical problems involving periodic potentials or elliptical shapes, and they were first introduced by French mathematician Charles Émile Mathieu in 1868 when analyzing the motion of elliptical membranes.

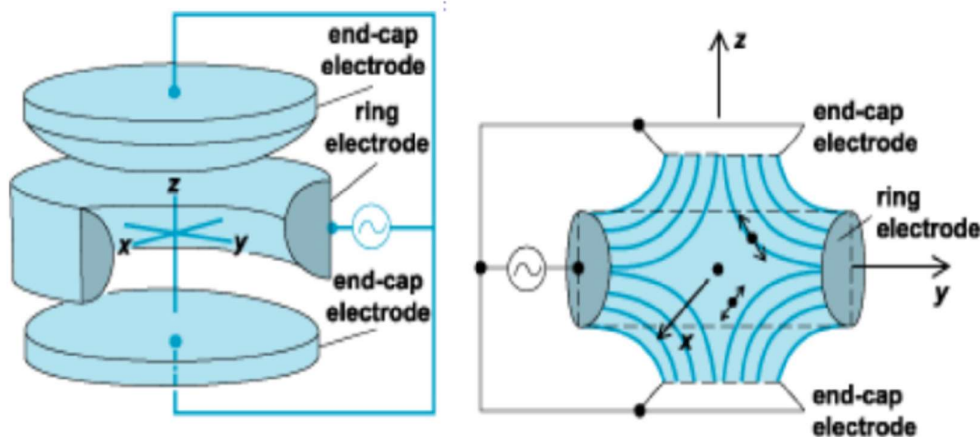


FIGURE 4.7 Electric Field Configurations in Paul Trap

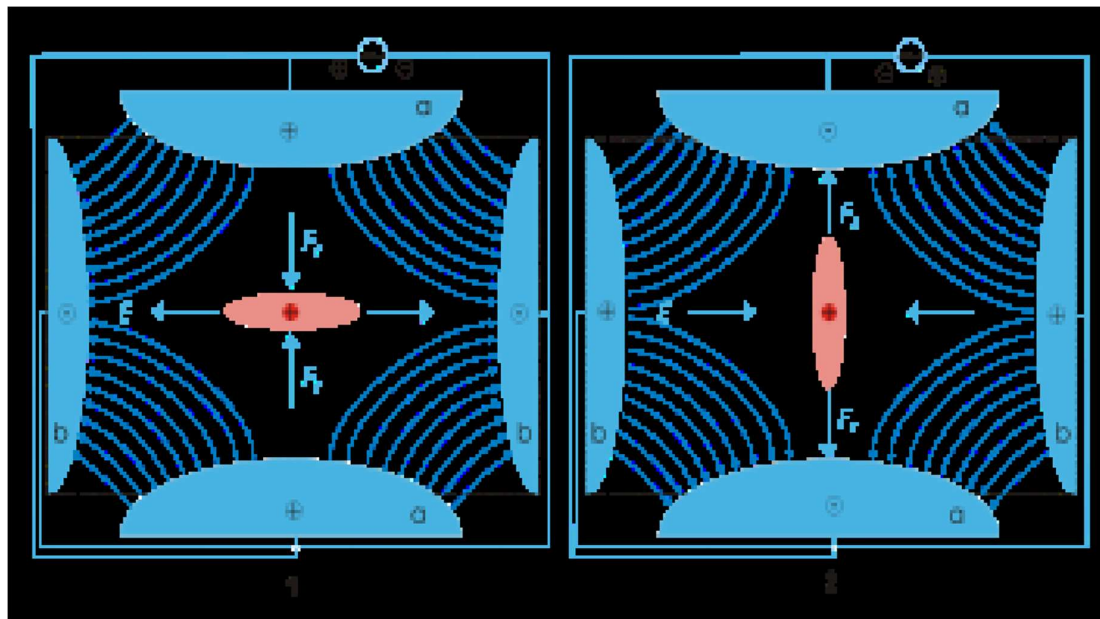


FIGURE 4.8 Alternating Electric Field

4.4 DETECTION SCHEMES

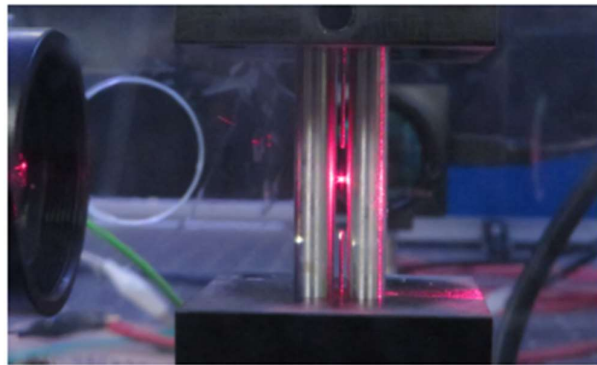


FIGURE 4.9 Photograph of scattered light from a trapped microsphere. A red laser beam (650 nm) is focused on the particle's position inside the trap. The scattered light from the particle can be seen even with naked eyes.

Even a simple LED torch is able to reveal the particles' position inside the trap. Nevertheless, we require a more accurate detection technique to obtain quantitative information about the particle motion. In our case, we are interested in the amplitude and frequency of the motion of the trapped particles. For this purpose, we have chosen to use back-focal-plane interferometry, which is characterized by high temporal and spatial resolution. Moreover, we use standard imaging to detect the relative position of the particles inside the trap. The aim of this section is to present the theory and implementation of these detection schemes.

4.4.1 LASER AND SPATIAL FILTER

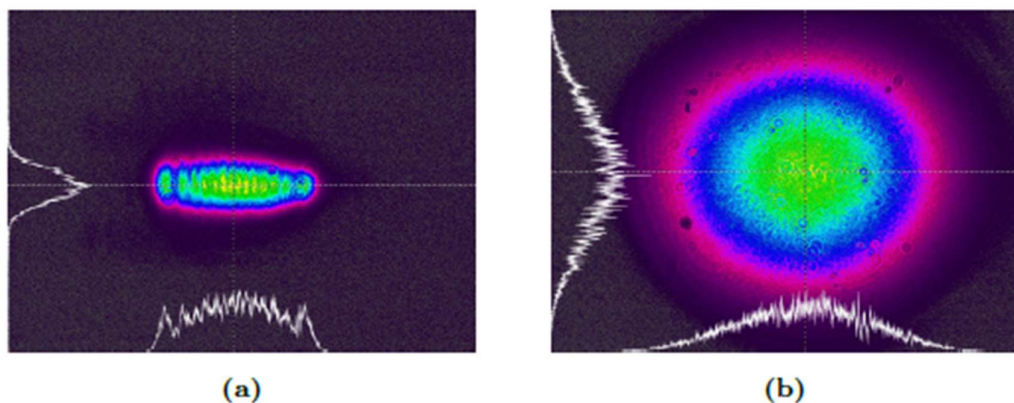


FIGURE 4.10: Transverse laser mode at the input a) and output b) of the spatial filter image on a beam profiler. A symmetric mode is important to guarantee equal efficiency in the detection of the lateral motion of the trapped particle in both transverse directions.

The laser used to illuminate the particles is a red diode laser at 650 nm. The intensity profile at the output of the laser head is spatially multimode (see Fig. (4.10)). In order to obtain a Gaussian profile, we assembled an optical spatial filter: this consists of two lenses ($f=30$ mm and $f=200$ mm) set in a confocal configuration. At the beam focus we place a 15 μm pinhole. After the spatial filter, the laser output power is reduced from 5mW to 2mW.

4.4.2 CAMERA DETECTION

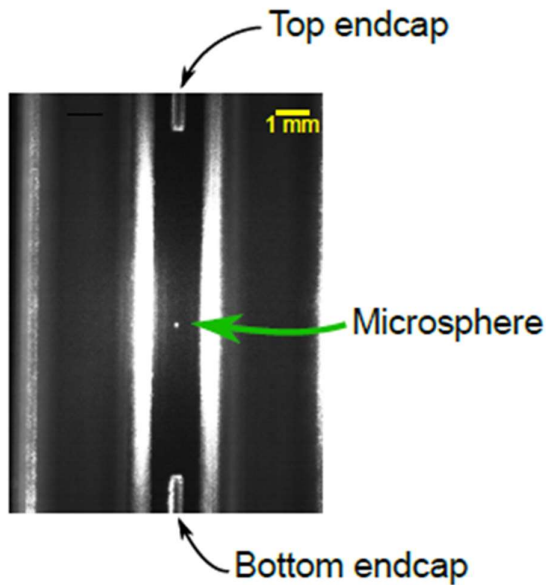


FIGURE 4.11: Image of a trapped microsphere taken with the CMOS camera with a resolution of 1024x1024 pixels.

In addition to interferometric measurements, we used a CMOS camera⁷ to detect the position of the particles inside the trap. A typical image of a trapped particle taken with the camera is shown in Fig. (4.11). The camera is able to detect both nanospheres and microspheres. A nanosphere's image typically extends for 3 pixels, a microsphere is 18 pixels in diameter instead (see Fig. (4.12)). In order to optimize the image quality, various settings of the sensor, including pixel rate (up to 41 MHz), exposure time and frames per second (up to 250 fps), are adjusted via the software of the camera.

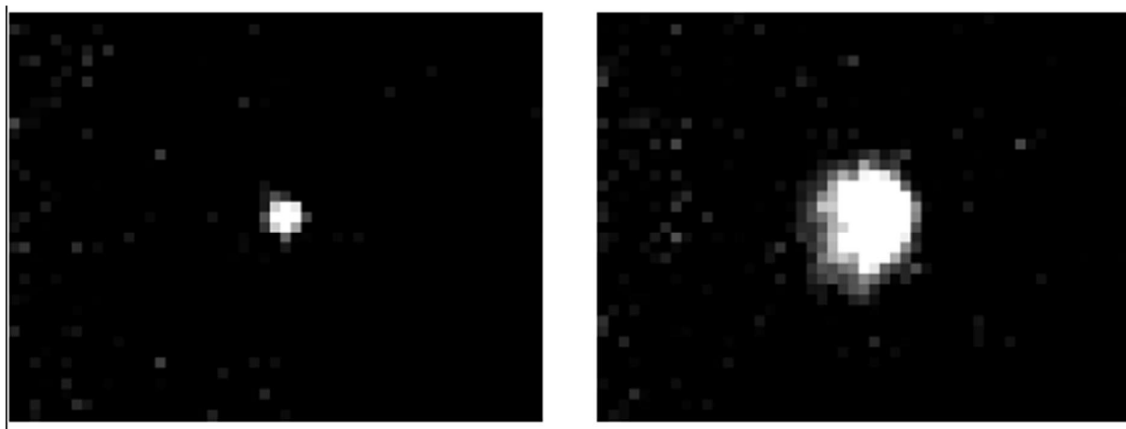


FIGURE 4.12 Nanosphere (a) and microsphere (b) scattered light recorded with the camera. For a comparison of their effective sizes, these images were taken with the same camera settings (exposure time, pixel rate, intensity gain, resolution).

Since the trap is mounted in the vertical position, the two orthogonal directions for optical access both lie on the table's plane. The camera was thus placed in the direction perpendicular to the laser beam (Fig. (4.13)), given that the principal axis is used for interferometric measurements with the photodiodes.

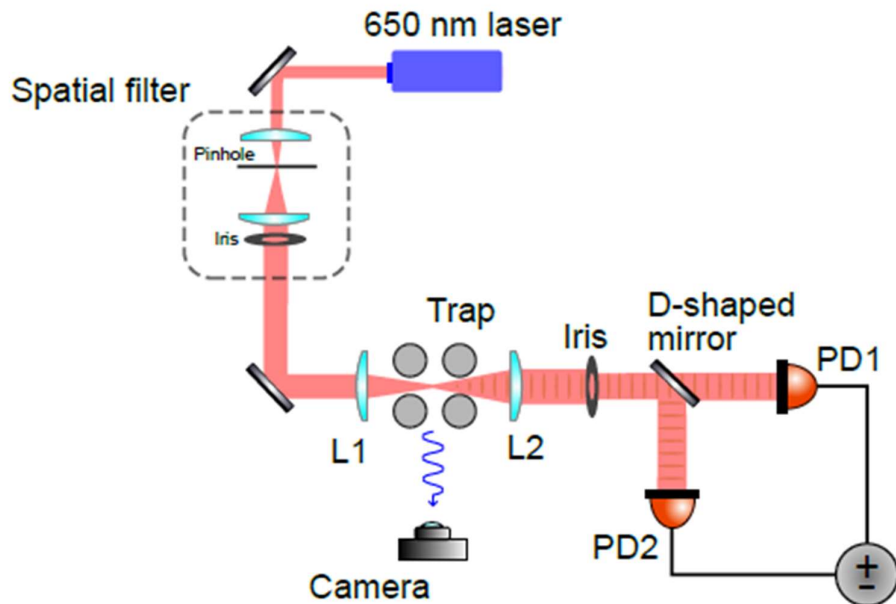


FIGURE 4.13 Schematic of the entire setup. The 650nm laser for imaging enters in the spatial filter that selects the TEM00 mode only. Then, the light is focused by the objective lens (L1) into the trapped particle. The scattered light from the particle is collected by the camera, which is placed at right angle with respect to the optical axis at the same altitude of the Paul trap. The sum of the scattered and the unscattered light is collimated by the condenser lens (L2), and then equally splitted by a D-shaped mirror. Each of the two beams leaving the D-shaped mirror goes to a pair of photodiodes (PD1 and PD2), which work in balanced configuration. An iris placed before the D-shaped mirror reduces the beam's diameter, ensuring the axial motion detection of the microsphere.

4.4.2.1 DISTANCE CALIBRATION

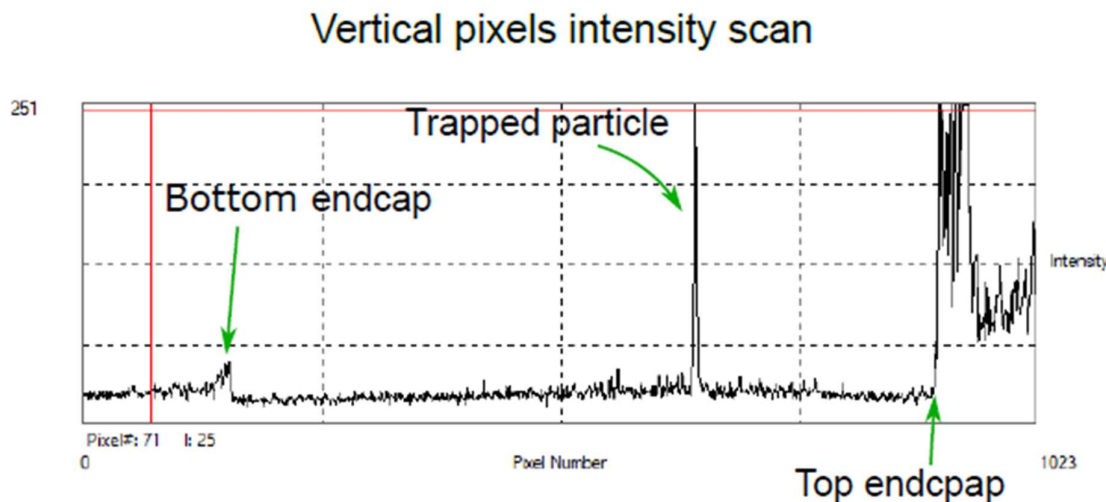
After a proper calibration, camera detection allows us to infer the absolute equilibrium position of the trapped particle within the electric field of the Paul trap, which in turn provides useful information about the charge state of the particle. Fig. (4.14) shows a pixel intensity profile along the vertical axis of the trap that intersects the endcap electrodes and the trapped microsphere. The distance calibration is made possible by the known size of the endcap electrodes (diameter of 0.4 mm). In this way, we can calculate the conversion factor between pixels and millimeters C:

$$C = \text{endcap diameter in (mm)} / \text{endcap diameter in (pixels)} = 0.0106 \pm 0.0001 \text{ mm/pixel}$$

4.5 DATA ANALYSIS TOOL

The electric signals coming from the photodiodes of the imaging system are connected to a Field Programmable Gate Array (FPGA) board. The two inputs of the board sample the analog inputs at a rate of 125 Msps with a resolution of 14 bit; the maximum input voltage is 20V.

FIGURE 4.14: This plot shows the pixel intensity (au) as a function of the pixel position along a vertical



line passing on the two endcaps. The graph is taken from the camera software.

The card is equipped with an open-source software package that provides an oscilloscope and a spectrum analyzer that we use to compute the power spectral density of the trapped particle motion.

4.6 MATERIALS REQUIRED

- ❖ A source of high voltage. We used a standard wall output and a 15X step-up transformer to achieve a working voltage of 2 kV AC at 60 Hz. High-voltage transformers might be difficult to find, and is perhaps the most challenging part of the set up.
- ❖ Current limiting resistors for the purpose of safety.
- ❖ An acrylic box. Our box's dimensions are 600*600*800.
- ❖ A Variac.
- ❖ Small particles to be trapped. We used plaster dust.
- ❖ A laser pointer to illuminate trapped particles. We used a 30mW laser.
- ❖ Copper wires.
- ❖ 2 metal spheres (1-2 cm diameter) to be used as electrodes. Small spoons may also be used if desired.
- ❖ High speed camera.

(Optional) Black spray paint and black construction paper.

(Optional) Wooden stand to mount electrodes.



(a)



(b)



(c)



(f)



(d)



(e)

FIGURE 4.15 Picture of components. (a) Spoons act as electrodes. (b) LASER light. (c) Camera. (d) Step-up transformer. (e) Thick copper wire for making ring shaped anode. (f) Capacitors and Resistors of different values.

4.7 SETUP

4.7.1 ACRYLIC BOX

The acrylic box serves two major purposes. The first is to isolate the system for the purpose of safety. We recommend constructing the acrylic box first so that it may be kept on top of the apparatus at all times except for when adjustments are made. The second purpose is to reduce air flow. We want to reduce the possibility that air currents could knock the particles out of the trap.



FIGURE 4.16 Acrylic box setup

First, the Variac is connected to wall voltage. The Variac allows us to gradually increase or decrease the voltage applied to the transformer. This gives us another layer of safety in the system, and it also allows us to test various aspects such as the minimum voltage needed to maintain the trapped particles. Next, the Variac is connected to the high-voltage transformer inside the acrylic box through the medium size hole. This will step up the voltage to the necessary minimum for trapping.

4.7.2 ELECTRODE SETUP

In this setup, there are two electrodes that we will set up. For the first electrode, solder the two metal spheres to both ends of a thin, stiff copper rod. Bend the rod into a U shape, fix the electrode in place, and establish an electrical connection of one wire from the transformer to the bent copper rod by either soldering it in place or wrapping the wire tightly around the copper rod. Cover the exposed wire with electrical tape.

For the second electrode, strip a thin metal wire of any insulation and bend it into a ring. Through the same procedure, electrically connect the metal wire to the wire coming from the transformer. Position the ring between the two metal spheres. Ideally, the diameter of the circle should be the same as the distance between the two metal spheres. Make sure that all wires are not in contact with one another.

In order to maintain the position of electrodes and wiring, a wooden stand or platform can be used. The hyperbolic electrodes are fixed to the wooden stand using glue and tape, and the ring electrode is affixed using glue.

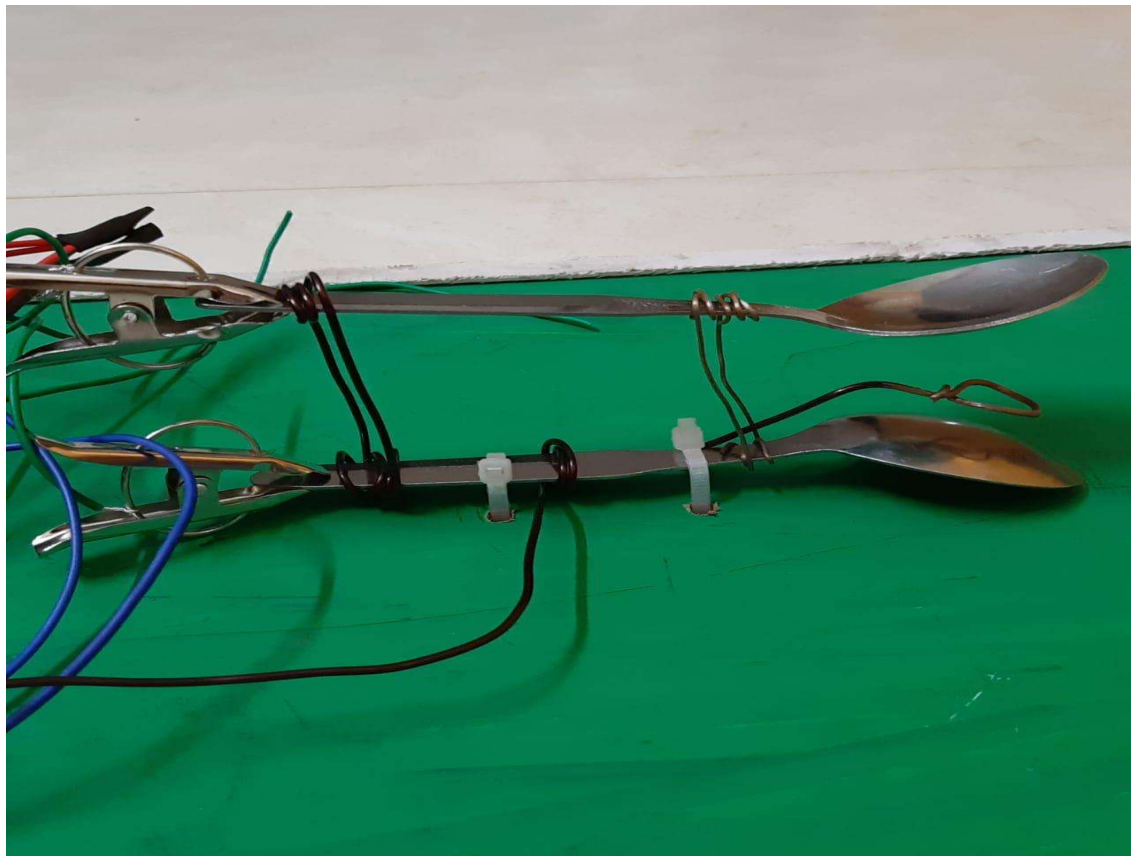


FIGURE 4.17 Electrode setup

CHAPTER 5

EXPERIMENTAL RESULTS & APPLICATIONS

5.1 CHARACTERIZATION OF THE TRAP AND LOADING METHODS

We first want to identify the parameters that influence the number of charges on the particles. This will allow us to find a protocol to load particles in a reproducible and systematic way. Nanospheres are loaded using electrospray (cf. Chap. (4.2.1)). Both the electrospray launch and capture by the Paul trap act as charge filters. Particles launched by electrospray are loaded with a variable number of elementary charges depending on various factors, mainly:

- ❖ Needle voltage
- ❖ Distance between needle and trap
- ❖ Initial concentration of the solution
- ❖ Shape and dimension of the particle

After launching, a broad distribution of charged particles is accelerated toward the trap by the electric field of the needle. However, not every particle gets trapped. Thus, the trap works as a charge-to-mass filter. Since it is possible to modify the trap acceptance by varying the RF field parameters, one can reconstruct the initial charge distribution of the electrospray source in terms of the trap parameters.

5.1.1 CHARGE OVER MASS MEASUREMENTS

After loading the trap with a single species, we measure its charge-to-mass ratio by scanning the endcap voltage while monitoring the axial position of the particle with the camera. Due to its charge, the trapped particle acts as a sensor of the static electric field produced by the electrodes, positioning itself where the electric force balances the gravitational pull:

$$mg = QE(z_{eq})$$

where g is the gravitational acceleration constant and $E(z_{eq})$ is the value of the static electric field produced by the end cap evaluated at the trap equilibrium position z_{eq} . The electric field generated within the trap has been calculated from computer simulation¹, and it is shown in Fig. (5.1). If z_{eq} is subsequently determined from camera imaging (cf. Chap.(4.3.3)), the charge-to-mass value of a single particle can be extrapolated.

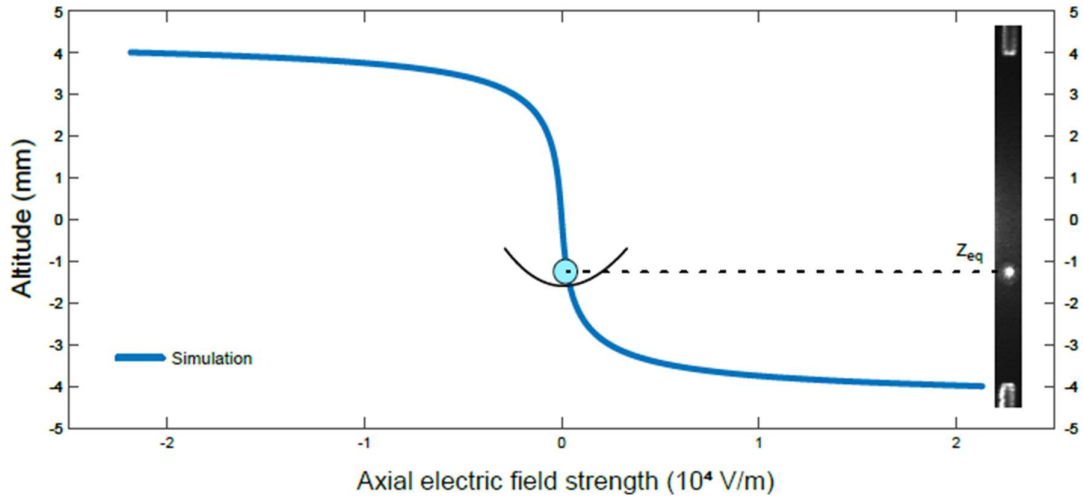


FIGURE 5.1: Computer simulation of the axial electric field of the trap with an endcaps voltage of 15V.

5.2 STABILITY DIAGRAMS

To trace the boundaries of the stability diagram of our system, we study the particle motion using camera imaging. Fig. (5.2) shows two camera frames of a particle trapped with a different RF field in each case. As soon as the parameters of the trap (voltages URF and frequency) exceed specific threshold values, a transition occurs that causes the amplitude of motion of the particle to increase. The system is said to be unstable whenever its elongated orbit starts to slowly drift out of the trap. Several trapping sessions showed that after this point is reached, the chances of losing the particle increase substantially. The set of all the observed points in the parameter space that give rise to instability form the stability boundary. The nanospheres and microspheres elongated orbit's extensions close to their respective stability boundaries are not constant in pixel number, so that the error associated with a single point in the stability diagram is estimated on a case by case basis.

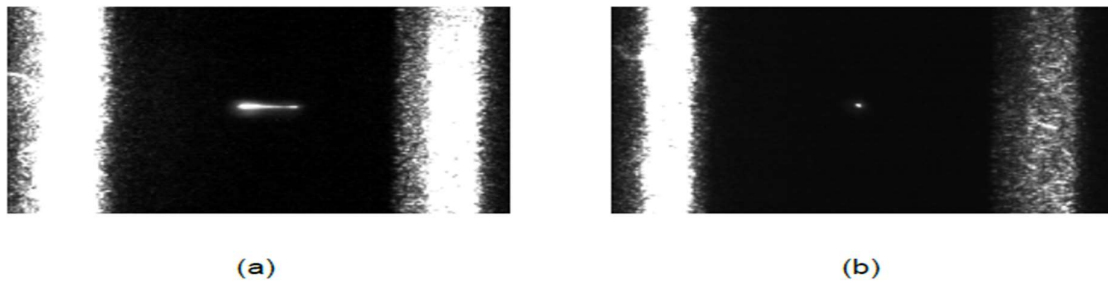


FIGURE 5.2 Unstable (a) vs. stable (b) motion of a microsphere inside the trap captured by the camera. The measures of voltage and frequency that label an unstable point is taken whenever the camera shows an increased orbit in pixels of about 10 times the stable case.

The stability boundary from the U_{RF} - \square space can be mapped into the more familiar a - q space via the linear trap equations of motion. Here a and q stand for

$$a = -\frac{4Q}{m\Omega} \left(\frac{U_{off}}{r_0^2} + \frac{U_{end}}{z_0^2} \right),$$

$$q = \frac{2QU_{RF}}{mr_0^2\Omega}$$

where U_{RF} is the AC voltage that drives the rod electrodes, which oscillates at frequency \square ; U_{end} and U_{off} are, respectively, the endcap voltage and the DC offset voltage applied to the rods; r_0 and z_0 are geometric parameters of the trap; and Q and m are the charge and the mass of the trapped particle, respectively.

In order to determine the stability diagram, the following procedure has been adopted for both nanospheres and microspheres:

- ❖ A single particle is loaded into the trap.
- ❖ The charge-to-mass ratio of the trapped particle is measured.
- ❖ Starting from a stable configuration, the offset voltage of the rod electrodes U_{off} is increased until an instability is reached.
- ❖ The offset voltage U_{off} is then lowered towards the next unstable boundary.
- ❖ Points 3 and 4 are repeated with several different values of the driving voltage U_{RF} .

The stability diagram is then obtained by transforming the set of all the instability coordinates in the plane U_{RF} - U_{off} to the a - q -plane.

The reason why the scanning is performed for U_{off} instead of U_{end} is that a is proportional to $U_{off}/r_0^2 + U_{end}/z_0^2$: Since the endcap separation z_0 is larger than the distance r_0 between rods, a larger range of ‘ a ’ can be covered by scanning the offset voltage rather than the axial field of the endcaps. Moreover, it has been found that the amplitude of the driving voltage accessible with our experimental setup cannot entirely cover the first stability zone. This

problem was circumvented by adjusting the drive frequency of the trap: because of the $1/\beta^2$ dependency of both a and q , lowering the frequency allows us to reach higher a and q values.

5.2.1 STABILITY DIAGRAM OF THE MICROPARTICLE

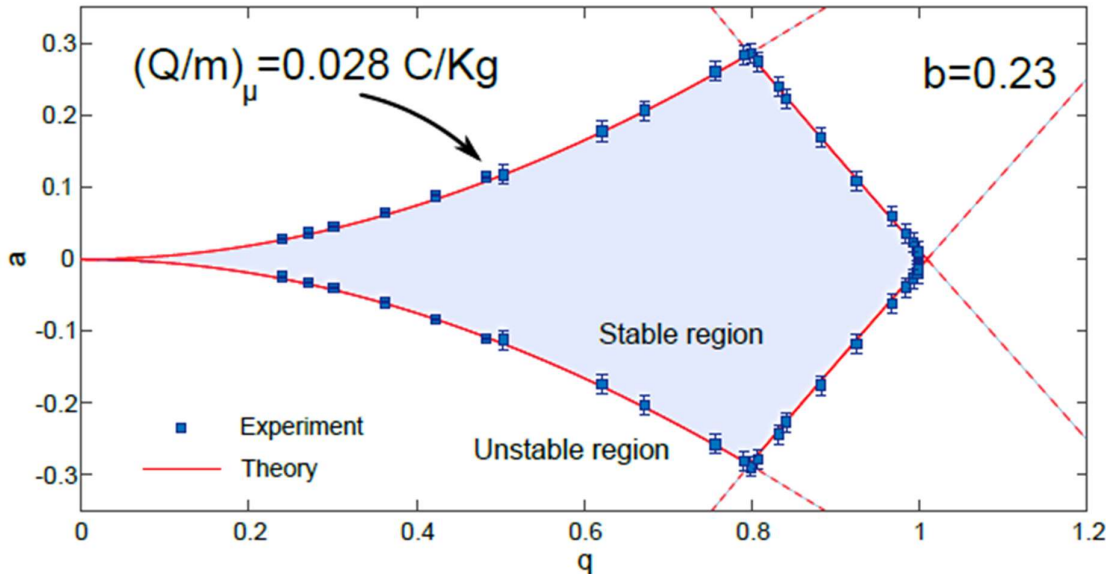


FIGURE 5.3 Measured stability diagram of a single $21.8 \pm 0.9 \mu\text{m}$ microsphere trapped in air at a fixed frequency $\Omega = 2\pi \times 290 \text{ Hz}$. Here the experimental data U_{off} and U_{RF} corresponding to unstable behavior were rescaled via Eq. (4.2.1) to their dimensionless parameters a and q in a way such that the charge-to-mass value of the microsphere $(Q/m)\mu$ is the theoretically calculated stability boundary (red solid line) for the case of trapping in air (b is obtained from Eq. (4.2.2)). For each point in the diagram, the error bar is estimated individually by observing whenever the trapped particle starts to slowly drift out of the trap. Precedent trapping sessions showed that after reaching this point the particle escapes from the trap.

The stability diagram of a trapped microsphere is depicted in Fig. (5.3). This microsphere has a measured charge-to-mass ratio of $Q/m(\text{simulation}) = 0.021 \pm 0.001 \text{ Ckg}^{-1}$ and was loaded and driven into the Paul trap at the drive frequency of $\Omega = 2\pi \times 290 \text{ Hz}$. The shown data are obtained from the values of U_{off} and U_{RF} corresponding to unstable behavior of the particle, then rescaled via Eq. (4.2.1) to their dimensionless parameters a and q in a way such that the charge-to-mass value of the microsphere $Q/m @ \mu$ is the theoretically calculated stability case of trapping in air. For this purpose, the dimensionless damping factor $b\mu$ used for calculating the theoretical stability boundary has been calculated from the Stokes formula

$$b_{\text{micro}} = \frac{6\pi\eta r_p}{m_p \Omega} = 0.23 \pm 0.02$$

where r_p is the radius of the particle, $n = 1.8 \times 10^{-5} \text{ kg m}^{-1} \text{ s}^{-1}$ is the dynamic viscosity of air at ambient pressure, and the error has been calculated from the uncertainty of the particle radius. A good matching between data and theoretical prediction is reached with $Q/m @ \mu = 0.028 \text{ C kg}^{-1}$, confirming the goodness of the independent estimate upon the electric field simulation inside the trap.

The diagram shows the typical shape of the first region of stability, due to the overlap of the stable operation parameters in both the x and y directions. The symmetry with respect to reflection across the $a = 0$ line suggests that the same instabilities occur if we either change the polarity of U_{off} or if we apply the offset voltage to the other diagonal pair of rod electrodes. The latter is a consequence of the linear trap symmetry.

The maximum q value belonging to the stable region of air trapping in Fig.(5.3) is larger than its vacuum counterpart $q_{\text{vacuum}}(\text{max}) = 0.9$. This is indeed a consequence of the air damping, which causes the enlargement of the stable region of the trap.

5.2.2 STABILITY DIAGRAM OF THE NANOPARTICLES

The stability diagram of a nanosphere with charge-to-mass ratio of $Q/m_{\text{simulation}}(n) = 10 \pm 1 \text{ C kg}^{-1}$ trapped at $\Omega(n) = 2\pi \times 10 \text{ kHz}$ as shown in Fig (5.4). The nanosphere has a larger charge-to-mass value than the microsphere, which leads to the possibility to explore higher values of q . In fact, the plot never shows a closed path to a maximum q value.

Since the size of the nanospheres (radius of 50 nm) is comparable with the mean free path of air molecules at ambient pressure, $l_{\text{mfp}} = 68 \text{ nm}$, kinetic theory corrections to the Stokes damping formula have to be used.

According to the results of Beresnev et al., the dimensionless damping parameter is given by,

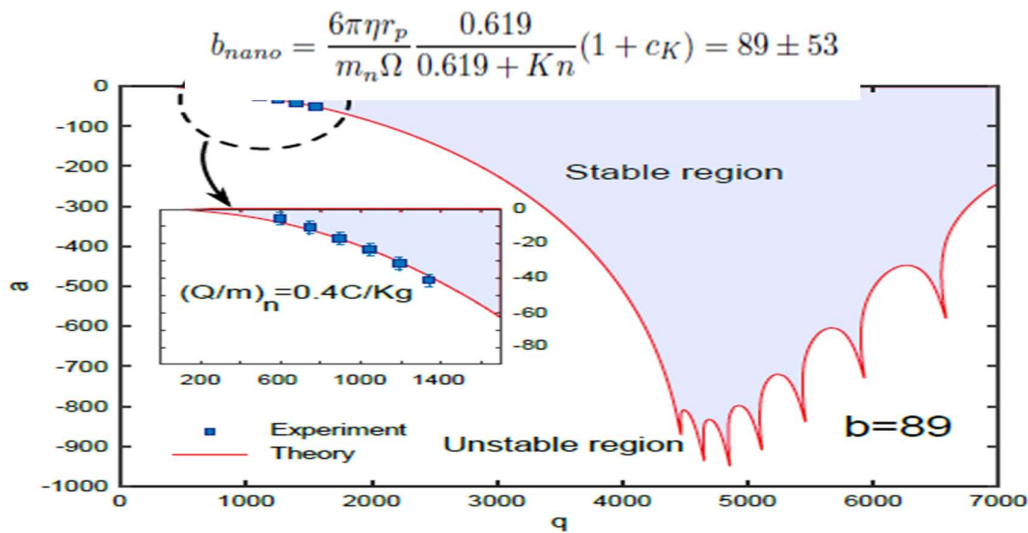


FIGURE 5.4: Measured stability diagram of a trapped nanosphere at frequency $\omega'' = 2\pi \times 10$ kHz. The red solid line represents a theoretical stability boundary calculated with a dimensionless damping factor $b = 89$. The experimental values of U_{off} and URF have been rescaled to their dimensionless counterparts a and q , obtaining a match with the theoretical prediction by using $Q/m(n) = 0.4Ckg^{-1}$.

where $Kn = l_{mfp}/rp$ is the Knudsen number, $c_K = (0.31Kn)/(0.785 + 1.152Kn + Kn^2)$ is a small positive function of Kn , and m and rp are the mass and the radius of the nanosphere, respectively. The very large uncertainty in b_{nano} reflects the factory declared uncertainty in nanosphere's diameter $2r_p = 0.10 \pm 0.03$ μm . As it was done for the microsphere case, the experimental points shown in Fig. (5.4) are rescaled in a way such that the data are superimposed with the theoretically predicted stability boundary for the case of $b_n = 89$. The match was obtained with $Q/m(n) = 0.4Ckg^{-1}$, in strong disagreement with the charge-to-mass ratio calculated upon the axial electric field simulation, which doesn't need a measurement of the particle radius in order to be performed, and thus results are more precise.

5.3 RESULTS

The trapped particles assemble and oscillate along the electric field lines of the system. These oscillations will be observed using a camera with high frame rate and slow-motion capabilities to record the trapped particle. Variation in input voltage with the help of variac reflected upon the movement of the particle. The movement of particles will start after a certain threshold value of voltage.

5.4 OBSERVATIONS

The trapped particles assemble and oscillate along the electric field lines of the system. In this setup, we have a restorative electric force that holds the particles in place. We noticed that the particles are more concentrated below the ring than above the ring. This is because gravity pulls the particles downward, which shifts the zero point of the system from the centre of the ring to slightly below the centre of the ring. This observation can also be attributed to the fact that our ring electrode is not perfectly circular, disturbing the symmetry of the system.

5.5 MINIMUM VOLTAGE REQUIREMENT

Below a certain voltage, gravity will overcome the electric forces holding the particles in place. The lowest voltage using which we were still able to trap the particles is at 40V from the Variac, which translates into around 600kV of post-transformer voltage. As we sweep the voltage

down towards 40V, we can see particles start to drop out of the trap. The distribution of particles starts to get smaller and more concentrated toward the centre, until all the particles drop out of the trap at around 600V.

5.6 OSCILLATIONS

In this system, the particles will constantly be bouncing up and down due to the oscillations of the electromagnetic forces. If you would like to observe these oscillations, find a camera with high frame rate and slow-motion capabilities to record the system. When you first observe the trapped particles, it appears as though there are several strands of dust that are immobile. However, looking at the video, it becomes apparent that there are only individual particles and not strands of particles. This means that the oscillations are happening so fast that each trapped particle appears as a strand to the naked eye.

5.7 CHALLENGES

- ❖ Bombardment of focused LASER beam on electrode.
- ❖ Placing ion particles in between the rings when alternating electric fields are applied.
- ❖ Regulation of applied voltage through variac.

5.8 APPLICATIONS

5.8.1 PAUL TRAP AS A MASS SPECTROMETER

Finally, we want to provide a basic introduction to the operation of a linear Paul trap as a charge-to mass spectrometer, which will be a useful tool for understanding the nanosphere loading mechanism with the electrospray ionization technique, the latter being known to generate a broad charge distribution among the launched particles. This method has been successfully used to estimate the charge-to-mass ratio of nanospheres in different configurations.

5.8.2 PRECISION MASS MEASUREMENT

Very precise values of g-factors and mass ratios have been obtained by measuring ion oscillation frequency in a Penning trap. The motional frequencies in Penning traps are related to cyclotron frequency $\omega_c = E_b/m$ and the basic idea for g-factor and mass measurements is a precise determination of the cyclotron frequency of the trapped particles.

5.8.3 QUANTUM JUMPS

As was stated before, the most impressive characteristic of ion traps is the possibility of carrying out experiments with a single ion. However, the preparation of a single ion in a trap can be difficult. To achieve this, the trap can be operated at the edge of the stability region while ions are loaded into 1.5 Applications of ion traps 51 the trap. Doing this, just a few ions will be trapped and, as the trap is almost unstable, the extra ions will be eventually lost. Alternatively, ions can also be created and loaded into the trap in a very small numbers using a well-characterized oven.

5.8.4 QUANTUM COMPUTATION

One of the most promising applications of ion traps is in the field of quantum computation. The ultimate aim of this field is the creation of a computational device where the data storage and their operations are performed by means of quantum properties. In this scheme, data units can be described by any two-state quantum mechanical system; one state represents 0 and the other represents 1. By analogy with a classical computer, these data units are commonly named qubits. As a qubit is defined as a quantum system, its state must be represented as a quantum superposition of its internal states.

5.8.5 FREQUENCY STANDARD

The most important possible application of cooled-trapped ions is the development of trapped ion frequency standards for both optical and microwaves regions. Ion traps offer the potential for achieving cooled ion species with very narrow resonances (with line widths a fraction of a Hertz, both in optical and microwave regions) with high accuracy and stability.

CONCLUSION AND OUTLOOK

We have shown that two-frequency operation of a Paul trap or quadrupole guide can provide a significant advantage when trapping species with dissimilar charge to mass ratios. In considering the stability of each species, we proposed an approach to finding suitable operating conditions within the multidimensional space. We have verified the predicted stability of the atomic ions experimentally and carried out numerical simulations of the two-frequency, two-species system. This previously unexploited mode of electrodynamic trapping, can be implemented on an existing apparatus and has general applicability. Electrodynamic confinement has many uses ranging from mass spectrometry of small molecules to the control of particles of dimensions hundreds of micrometres. We consider two broad categories of prospective applications: detection of heavy ions via their effect on fluorescing atomic ions, and reactions of cold molecular ions in cold (bio-)chemistry. Detection of ions via their effect on fluorescing atomic ions being excited with laser light is used for dark ions such as molecules, or atomic ions with transitions at inconvenient wavelengths. Our results show how to extend this detection technique to massive ions with lower charge-to-mass ratios than atomic ions. This can be used in mass spectrometry for the non-destructive detection of individual molecular ions at a low count rate. Moreover, an intrinsic part of mass spectrometry is fragmentation, i.e., observing the breaking apart of a large biological complex, and the two-frequency scheme enables such investigation of single biomolecular complexes without ensemble averaging. The efficient, non-destructive detection of biomolecular ions could be followed by controlled deposition of mass-selected particles on a surface for further analysis by other techniques. It has also been suggested that a chain of atomic and molecular ions can act as a conveyor belt to carry the dark molecular ions into the focus of an x-ray laser for destructive measurements, as demonstrated in experiments with Mg^+ and MgH^+ which have similar charge-to-mass ratios. Our method opens the way to working with much heavier biomolecular ions. Paul traps are used to investigate chemical reactions of ions at low temperatures, and two-frequency operation allows much heavier species to be used without a large spatial separation. This application is closely related to the use of two frequencies for the confinement of antimatter where the creation of overlapping clouds of positrons and antiprotons leads to the formation of antihydrogen atoms; work towards this technically challenging goal is ongoing.

APPENDICES

APPENDIX A

NUMERICAL CODE FOR THE STABILITY DIAGRAMS

A numerical code for the evaluation of the stability diagrams shown in the main text was written using the software Matlab.

```
function beta = beta_p(a, p, q)

n = 3;
h = 10;

d = 2 * h + 2 * (n - 2) + 5;
r = (d - 1) / 2;

A = eye(d) - q.* diag(1./(a - (2 * (-r : r - 1)).^2), 1) - q.* diag(1./(a - (2 * (-r + 1 : r)).^2), -1) -
p.* diag(1./(a - (2 * (-r : r - n)).^2), n) - p.* diag(1./(a - (2 * (-r + n : r)).^2), -n);

detA = det(A);

if (mod(sqrt(abs(a)), 2) == 0)

beta = 1/ pi*acos(2*det(eye(d)-q.*diag(1./(a-(1+2*(-r:r-1)).^2),1)-q.*diag(1./(a-(1+2*(-r+1:r)).^2),-1)-p.*diag(1./(a-(1+2*(-r:r-n)).^2), n)-p.* diag(1./(a-(1+2 * (-r+n:r)).^2),-n))-1);

else
beta = 2/ pi * asin(sqrt(detA * (sin(pi /2.* sqrt(a))^2)));
end
end

x = [0 : 0:05 : 50];%arange
y = [0 : 0:05 : 25];%qrange
```

```
for h = 1 : length(x)
    for j = 1 : length(y)
        mat(j, h) = beta_p(x(h), 0, y(j));
    end
end

[X, Y] = meshgrid(y, x);
figure;

[C, r] = contour(X, Y, real(mat'), 'k');

w = r.LevelList;
r.LevelList = [1, 0.001];

holdon
```

BIBLIOGRAPHY

- [1] V. Braginski and A. Manukin, \Ponderomotive effects of electromagnetic radiation," Sov. Phys. JETP, vol. 25, no. 4, pp. 653\{655, 1967}.
- [2] B. Abbott et al, \Observation of a kilogram-scale oscillator near its quantum ground state," New Journal of Physics, vol. 11, no. 7, p. 073032, 2009.
- [3] T. A. Palomaki, J. W. Harlow, J. D. Teufel, R. W. Simmonds, and K. W. Lehnert, \Coherent state transfer between itinerant microwave fields and a mechanical oscillator," Nature, vol. 495, p. 210, Mar 2013.
- [4] J. Chan, T. P. M. Alegre, A. H. Safavi-Naeini, J. T. Hill, A. Krause, S. Groblacher, M. Aspelmeyer, and O. Painter, \Laser cooling of a nanomechanical oscillator into its quantum ground state," Nature, vol. 478, p. 89, Oct 2011.
- [5] T. P. Purdy, D. W. C. Brooks, T. Botter, N. Brahms, Z.-Y. Ma, and D. M. Stamper-Kurn, \Tunable cavity optomechanics with ultracold atoms," Phys. Rev. Lett., vol. 105, p. 133602, Sep 2010.
- [6] O. Romero-Isart, A. C. Panzer, M. L. Juan, R. Quidant, N. Kiesel, M. Aspelmeyer, and J. I. Cirac, \Optically levitating dielectrics in the quantum regime: Theory and protocols," Phys. Rev. A, vol. 83, p. 013803, Jan 2011.
- [7] A. C. Panzer, O. Romero-Isart, and J. I. Cirac, \Optomechanics assisted by a qubit: From dissipative state preparation to many-partite systems," Phys. Rev. A, vol. 88, p. 033804, Sep 2013.
- [8] D. Trypogeorgos and C. J. Foot, \Trapping different species in ion traps using multiple radio frequencies," Phys. Rev. A, vol. 94, p. 023609, Aug 2016.
- [9] A. Siegman, Lasers. University Science Books, 1986.
- [10] C. W. Gardiner and P. Zoller, Quantum Noise. Springer, second ed., 2000.
- [11] M. Aspelmeyer, T. J. Kippenberg, and F. Marquardt, \Cavity optomechanics," Rev. Mod. Phys., vol. 86, pp. 1391\{1452, Dec 2014.
- [12] D. E. Chang, C. A. Regal, S. B. Papp, D. J. Wilson, J. Ye, O. Painter, H. J. Kimble, and P. Zoller, \Cavity opto-mechanics using an optically levitated nanosphere," Proceedings of the National Academy of Sciences, vol. 107, no. 3, pp. 1005\{1010, 2010.
- [13] J. Millen, P. Z. G. Fonseca, T. Mavrogordatos, T. S. Monteiro, and P. F. Barker, \Cavity cooling a single charged levitated nanosphere," Phys. Rev. Lett., vol. 114, p. 123602, Mar 2015.
- [14] J. Schwinger, The Theory of Obstacles in Resonant Cavities and Wave Guides. Report (Massachusetts Institute of Technology. Radiation Laboratory), Radiation Laboratory, Massachusetts Institute of Technology, 1943.

- [15] L. Novotny and B. Hecht, *Principles of Nano-Optics*. Cambridge University Press, 2 ed., 2012.
- [16] A. A. Clerk and F. Marquardt, *Basic Theory of Cavity Optomechanics*, pp. 5{23. Berlin, Heidelberg: Springer Berlin Heidelberg, 2014.
- [17] J. Gieseler, B. Deutsch, R. Quidant, and L. Novotny, \Subkelvin parametric feedback cooling of a laser-trapped nanoparticle," *Phys. Rev. Lett.*, vol. 109, p. 103603, Sep 2012.
- [18] N. Kiesel, F. Blaser, U. Delic, D. Grass, R. Kaltenbaek, and M. Aspelmeyer, \Cavity cooling of an optically levitated submicron particle," *Proceedings of the National Academy of Sciences*, vol. 110, no. 35, pp. 14180{14185, 2013.
- [19] T. S. Monteiro, J. Millen, G. A. T. Pender, F. Marquardt, D. Chang, and P. F. Barker, \Dynamics of levitated nanospheres: towards the strong coupling regime," *New Journal of Physics*, vol. 15, no. 1, p. 015001, 2013.
- [20] J.-M. Pirkkalainen, S. U. Cho, F. Massel, J. Tuorila, T. T. Heikkila, P. J. Hakonen, and M. A. Sillanpaa,\Cavity optomechanics mediated by a quantum two-level system," *Nature Communications*, vol. 6, p. 6981, Apr 2015.
- [21] A. B. Mundt, A. Kreuter, C. Becher, D. Leibfried, J. Eschner, F. Schmidt-Kaler, and R. Blatt, \Coupling a single atomic quantum bit to a high nesse optical cavity," *Phys. Rev. Lett.*, vol. 89, p. 103001, Aug 2002.
- [22] A. Stute, B. Casabone, P. Schindler, T. Monz, P. O. Schmidt, T. E. Northup, and R. Blatt, \Tunable ion-photon entanglement in an optical cavity," *Nature*, vol. 485, p. 482, May 2012.
- [23] E. T. Jaynes and F. W. Cummings, \Comparison of quantum and semiclassical radiation theories with application to the beam maser," *Proceedings of the IEEE*, vol. 51, no. 1, pp. 89{109, 1963}.
- [24] S. Haroche and J.-M. Raimond, *Exploring the quantum: atoms, cavities, and photons*. Oxford University press, 2006.
- [25] C. K. Law and J. H. Eberly, \Arbitrary control of a quantum electromagnetic eld," *Phys. Rev. Lett.*, vol. 76, pp. 1055{1058, Feb 1996.
- [26] W. Paul, \Electromagnetic traps for charged and neutral particles," *Rev. Mod. Phys.*, vol. 62, pp. 531{540, Jul 1990}.
- [27] S. I. Kopnin, T. I. Morozova, and S. I. Popel, \Electron beam action and high charging of dust particles," *IEEE Transactions on Plasma Science*, vol. PP, no. 99, pp. 1{3, 2017.
- [28] S. Schlemmer, J. Illemann, S. Wellert, and D. Gerlich, \Nondestructive high-resolution and absolute mass determination of single charged particles in a three-dimensional quadrupole trap," *Journal of Applied Physics*, vol. 90, no. 10, pp. 5410{5418, 2001.

- [29] C. J. Foot, D. Trypogeorgos, E. Bentine, A. Gardner, and M. Keller, 'Two-frequency operation of a Paul trap to optimise confinement of two species of ions," arXiv:1801.00424, 2018.
- [30] D. Leibfried, R. Blatt, C. Monroe, and D. Wineland, 'Quantum dynamics of single trapped ions," Rev. Mod. Phys., vol. 75, pp. 281{324, Mar 2003.
- [31] P. Ghosh, Ion Traps. Clarendon Press, 1995.
- [32] M. Abramowitz, Handbook of Mathematical Functions, With Formulas, Graphs, and Mathematical Tables. Dover Publications, Incorporated, 1974.
- [33] 'Dynamical stability of a pendulum when its point of suspension vibrates," in Collected Papers of P.L. Kapitza (D. T. Haar, ed.), pp. 714 { 725, Pergamon, 1965.
- [34] L. D. Landau and E. M. Lifshitz, Mechanics. Pergamon Press: Oxford, 1969.
- [35] H. C. Nagerl, C. Roos, D. Leibfried, H. Rohde, G. Thalhammer, J. Eschner, F. Schmidt-Kaler, and R. Blatt, 'Investigating a qubit candidate: Spectroscopy on the S1=2 to D5=2 transition of a trapped calcium ion in a linear Paul trap," Phys. Rev. A, vol. 61, p. 023405, Jan 2000.
- [36] S. R. Jefferts, C. Monroe, A. S. Barton, and D. J. Wineland, 'Paul trap for optical frequency standards," IEEE Transactions on Instrumentation and Measurement, vol. 44, pp. 148{150, April 1995.
- [37] R. Alheit, S. Kleineidam, F. Vedel, M. Vedel, and G. Werth, 'Higher order non-linear resonances in a Paul trap," International Journal of Mass Spectrometry and Ion Processes, vol. 154, no. 3, pp. 155 {169, 1996.
- [38] W. M. Itano and D. J. Wineland, 'Laser cooling of ions stored in harmonic and penning traps," Phys. Rev. A, vol. 25, pp. 35{54, Jan 1982.
- [39] F. G. Major and H. G. Dehmelt, 'Exchange-collision technique for the rf spectroscopy of stored ions," Phys. Rev., vol. 170, pp. 91{107, Jun 1968.
- [40] T. Li, S. Kheifets, and M. G. Raizen, 'Millikelvin cooling of an optically trapped microsphere in vacuum," Nature Physics, vol. 7, p. 527 EP, Mar 2011.
- [41] V. Jain, J. Gieseler, C. Moritz, C. Dellago, R. Quidant, and L. Novotny, 'Direct measurement of photon recoil from a levitated nanoparticle," Phys. Rev. Lett., vol. 116, p. 243601, Jun 2016.
- [42] N. McLachlan, Theory and application of Mathieu functions. Clarendon Press, 1947.
- [43] T. Hasegawa and K. Uehara, 'Dynamics of a single particle in a Paul trap in the presence of the damping force," Applied Physics B, vol. 61, pp. 159{163, Aug 1995.

- [44] N. V. Konenkov, M. Sudakov, and D. J. Douglas, 'Matrix methods for the calculation of stability diagrams in quadrupole mass spectrometry,' *Journal of the American Society for Mass Spectrometry*, vol. 13, pp. 597{613, Jun 2002.
- [45] X. Chu, M. Holzki, R. Alheit, and G. Weitha, 'Observation of high-order motional resonances of an ion cloud in a Paul trap,' *International Journal of Mass Spectrometry and Ion Processes*, vol. 173, no. 1, pp. 107 { 112, 1998.
- [46] M. A. N. Razvi, X. Z. Chu, R. Alheit, G. Werth, and R. Blumel, 'Fractional frequency collective parametric resonances of an ion cloud in a Paul trap,' *Phys. Rev. A*, vol. 58, pp. R34{R37, Jul 1998.
- [47] X. Zhao, V. L. Ryjkov, and H. A. Schuessler, 'Parametric excitations of trapped ions in a linear rf ion trap,' *Phys. Rev. A*, vol. 66, p. 063414, Dec 2002.
- [48] N. Leefer, K. Krimmel, W. Bertsche, D. Budker, J. Fajans, R. Folman, H. Haffner, and F. Schmidt-Kaler, 'Investigation of two-frequency Paul traps for antihydrogen production,' *Hyperne Interactions*, vol. 238, p. 12, Dec 2016.

